Geomechanical unloading behaviour of Boom clay for excavations

Master of Science Thesis

Alexander Stefan Greeuw

August 3, 2015

Graduation committee:

prof. dr.	M.A. Hicks	Chairman
		Delft University of Technology
ir.	H.J. Lengkeek	Daily Supervisor
		Witteveen+Bos B.V.
dr. ir.	R.B.J. Brinkgreve	Supervisor department of Geo-Engineering
		Delft University of Technology
dr. ir.	K.J. Bakker	Supervisor department of Hydraulic Engineering
		Delft University of Technology

Acknowledgements

I would like to express my gratitude to my daily supervisor ir. Arny Lengkeek, whose expertise, deep interest in geo-engineering and experience guided me throughout my graduation project. I also must acknowledge Professor Dr Michael Hicks for presiding the graduation committee, dr. ir. Ronald Brinkgreve for his expert knowledge of numerical modelling and his extensive feedback on my work and dr. ir. Klaas Jan Bakker for his critical questions. A special mention to my father, who practically functioned as an extra supervisor, for his comprehensive guidance and recommendations on the interpretation of laboratory tests.

Witteveen+Bos provided the opportunity to work on the Oosterweel trial excavation. This was an unique full scale experiment with valuable data, which I greatly appreciated. I would like to thank ir. drs. Richard de Nijs for explaining all the details of the full scale experiment and ir. Jan Ruigrok for his valuable advice on the numerical model. Additionally the support and expertise of the other employees at Witteveen+Bos contributed to a very pleasant graduation project.

Various students and members of the academic staff have aided me throughout my years at the university. You have provided interesting lectures, discussions and countless essential coffee breaks, which were highly appreciated. Without you this work would not have been here today.

Finally I would like to thank my friends and family, for emphasising the importance of education and their contributions in various ways. Most importantly, I am very grateful to Floor for her patience and continuous support during the most challenging period of my studies.

Summary

This thesis describes the geomechanical unloading behaviour of Boom clay for excavations. The Boom clay is of specific interest for the completion of the motorway ring around Antwerp. Many deep excavations in the Boom clay have to be performed, but the clay's behaviour when unloaded is not fully understood to date. To gain better understanding of this behaviour a full scale trial excavation in Oosterweel, the west district of Antwerp, was performed. This resulted in unique field measurements on the Boom clay's unloading behaviour.

Besides the trial excavation numerous oedometer and triaxial tests were performed, with unloading/reloading steps. From these tests geotechnical and numerical parameters were determined. These parameters were used in the numerical calculations, which were validated with the field measurements.

For the numerical modelling of the trial excavation two numerical models have been used: the Hardening Soil model with small strain stiffness (HSs) and the Generalised Hardening Soil (GHS) model. The numerical calculations have been performed with an axisymmetric approach, which was acceptable due to the octagonal shape of the trial excavation. It was found that the influence of small strain stiffness is important to model the displacements correctly.

Both the HSs or GHS model provide a realistic approximation of the field measurements from the trial excavation. The pore water pressures, soil and sheet pile displacements are satisfactory modelled. It is important to consider the reduction of the minor principle stress when numerically modelling an excavation with HSs or GHS. This stress change greatly influences the stiffness moduli, resulting in unrealistic displacements. This was overcome by removing the stress dependency ($m = 0$) from the top layer.

The monitoring of the pore water pressures displayed a more permeable top layer of the Boon clay. The field measurements displayed an interesting difference between pore pressures measured by the piezometer tubes and the BAT-senors in the Boom clay. Suction was measured in the latter, but not in the piezometer tubes. This presumably shows that the undrained behaviour is not captured in piezometer tubes.

The long-term behaviour of the Boom clay remains a challenging point. It is recommended that laboratory oedometer tests are performed, lasting several months after the unloading steps. Additionally it is highly recommended to monitor the trial excavation in its current state for at least a year. This could provide crucial information on the long-term behaviour of the Boom clay.

Contents

List of figures

List of tables

List of Symbols

Symbol	Definition
Acronyms	
BK	Boomse Klei, the Boom Clay
Bm	Boom formation
CPT	Cone Penetration Test
CRS	Constant Rate of Strain
DSS	Direct Simple Shear
ESP	Effective Stress Path
GHS	Generalised Hardening Soil
HSs	Hardening Soil with small strain stiffness
Ma	Mega-annum
MC	Mohr-Coulomb
NC	Normally Consolidated
OC	Over Consolidated
OCR	Over Consolidation Ratio
OED	Oedometer
PP	Pocket Penetrometer
RoTS	Rechter oever Tunnel Specialisten
SBPM	Self Boring Pressure Meter
SCK	Studie Centrum voor Kernenergie
SEM	Scanning Electron Microscope
SHANSEP	Stress History And Normalised Soil Engineering Properties
SV	Shear Vane
TA	Tri-Axial
TAW	Tweede Algemene Waterpassing
TSP	Total Stress Path
UDSM	User Defined Soil Model
W+B	Witteveen+Bos

Symbol	Definition	Dimension	Unit
Latin letters			
A	$c' \times cot\ \varphi'$	$ML^{-1}T^{-2}$	kPa
c'	Effective cohesion	$ML^{-1}T^{-2}$	kPa
c_v	Consolidation coefficient	L^2T^{-1}	m^2/s
C_{air}	Compressibility of air	LT^2M^{-1}	kPa^{-1}
C_v	Compressibility of voids	LT^2M^{-1}	kPa^{-1}
C_w	Compressibility of water	LT^2M^{-1}	kPa^{-1}
C_{sk}	Compressibility of water	LT^2M^{-1}	kPa^{-1}
CR	(Virgin) Compression Ratio	$-$	-
e	Void ratio	$-$	-

Symbol	Definition	Dimension	Unit
Latin letters			
E_{50}	Secant stiffness for drained TA test	$ML^{-1}T^{-2}$	MPa
E_{oed}	Tangent oedometer stiffness primary loading	$ML^{-1}T^{-2}$	MPa
E_{ur}	Unloading/reloading stiffness	$ML^{-1}T^{-2}$	MPa
G_0	Inital shear modulus	$ML^{-1}T^{-2}$	MPa
G_s	Secant shear modulus	$ML^{-1}T^{-2}$	MPa
G_t	Tangent shear modulus	$ML^{-1}T^{-2}$	MPa
k	Permeability coefficient	LT^{-1}	m/s
K	Earth pressure coefficient	–	-
K_0	Coefficient of lateral earth pressure at rest	–	-
LI	Liquidity Index	–	%
LL	Liquid Limit	–	%
n	Porosity	–	%
p_{ref}	Reference stress	$ML^{-1}T^{-2}$	kPa
PI	Plasticity Index	–	%
PL	Plastic Limit	–	%
POP	Pre-Overburden Pressure	$ML^{-1}T^{-2}$	kPa
R_f	Failure ratio	–	-
RR	Recompression Ratio	–	-
s	$(\sigma_1 + \sigma_3)/2$	$ML^{-1}T^{-2}$	kPa
s_f	Peak shear strength	$ML^{-1}T^{-2}$	kPa
s_r	Residual shear strength	$ML^{-1}T^{-2}$	kPa
s_u	Undrained shear strength	$ML^{-1}T^{-2}$	kPa
t	$(\sigma_1 - \sigma_3)/2$	$ML^{-1}T^{-2}$	kPa
u	Pore water pressure	$ML^{-1}T^{-2}$	kPa
w	Water content	–	%
Greek letters			
γ	Shear strain	–	-
$\gamma_{0.7}$	Shear strain at which $G_s = 0.722G_0$	–	-
$\gamma_{cut-off}$	Cut-off shear strain	$ML^{-2}T^{-2}$	kN/m^3
γ_{sat}	Saturated unit weight	$ML^{-2}T^{-2}$	kN/m^3
γ_{unsat}	Unsaturated unit weight	$ML^{-2}T^{-2}$	kN/m^3
γ_w	Unit weight of water	$ML^{-2}T^{-2}$	kN/m^3
ε_1	Major principle strain	–	-
ε_h	Horizontal strain	–	-
ε_{sw}	Strain from swelling	–	-
ε_v	Vertical strain	–	-
ν	Poisson's ratio	–	-
ν_u	Undrained Poisson's ratio	–	-
ν_{ur}	Unloading/reloading Poisson's ratio	–	-
σ	Normal stress	$ML^{-1}T^{-2}$	kPa
σ_1	Major principle stress	$ML^{-1}T^{-2}$	kPa
σ_2	Intermediate principle stress	$ML^{-1}T^{-2}$	kPa
σ_3	Minor principle stress	$ML^{-1}T^{-2}$	kPa
σ'_c	Effective confining pressure	$ML^{-1}T^{-2}$	kPa
σ'_p	Effective preconsolidation stress	$ML^{-1}T^{-2}$	kPa
σ'_v	Vertical effective stress	$ML^{-1}T^{-2}$	kPa
φ'	Effective friction angle	–	$^\circ$
ψ	Dilatancy angle	–	$^\circ$

Chapter 1

Introduction

The flow of traffic in and around Antwerp has been troublesome for years. Daily traffic jams have been the cause to develop a mobility master plan which completes the motorway ring around Antwerp. This plan has been approved by the Flemish government in December 2000, but construction has not started to date. A big challenge for this project are the deep excavations in the Boom clay. The Boom clay has been investigated extensively, but its response in unloading is not fully understood. The geomechanical behaviour plays a significant role for the stability and deformations of these excavations. Thorough understanding of this behaviour is necessary to ensure a safe and efficient design.

Therefore Witteveen+Bos (W+B) designed a trial excavation in Oosterweel, the west district of Antwerp. This trial excavation is used to measure the actual behaviour of the Boom clay in a deep excavation. Besides the trial excavation numerous laboratory tests are performed. This has resulted in an abundance of unique data on the Boom clay.

1.1 Oosterweel trial excavation

Figure 1.1 displays the top view of the Oosterweel trial excavation. The excavation is approximately 25 metres deep and it is excavated to the Boom clay layer. The width of the trial excavation is 20 metres.

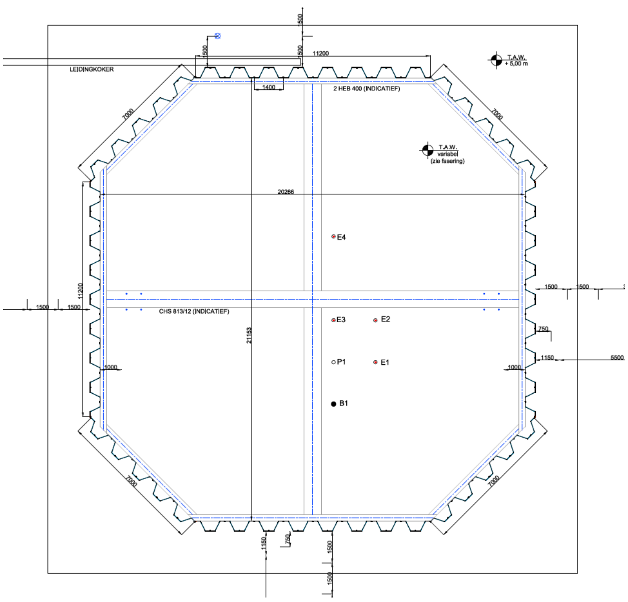

Figure 1.1: Top view of the Oosterweel trial excavation with location of measuring equipment, the folded lines indicate the sheet piles.

A global overview of the excavation phases is shown in Figure 1.2. All excavation steps have been performed as a dry excavation, with struts installed approximately every 5 metres. The light coloured top layers are mainly sands and the dark layer at the bottom is the Boom clay. Measuring equipment for the pore water pressures, displacements and sheet pile deformations were installed in and around the trial excavation.

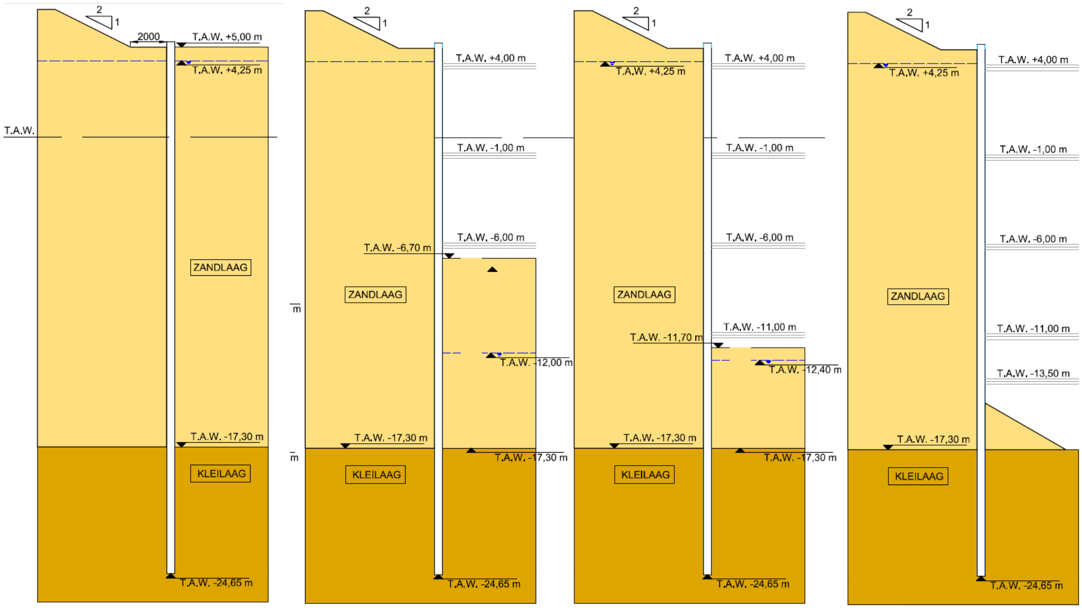

Figure 1.2: Simplified visualisation of the construction stages.

1.2 Research Goals

The trial excavation presents an excellent opportunity to further investigate and comprehend the Boom clay. The research goal of this MSc thesis is to *predict geomechanical unloading behaviour of Boom clay for excavations*.

To reach this research goal the following objectives are specified:

- To evaluate the Boom clay's geological setting and existing calculation methods
- To determine geotechnical and numerical Boom clay parameters
- To process and interpret the field measurements from the Oosterweel trial excavation

1.3 Thesis outline

This report commences with a selection of reference literature on the Boom clay in Chapter 2, where mainly the geology and geotechnical parameters are addressed. These will be compared to the derived parameters from the laboratory tests in Chapter 3. Chapter 4 specifies the numerical model and parameters and Chapter 5 the results from the numerical calculation. Chapter 6 presents the interpretation of the field measurements and a comparison with numerical calculations on the trial excavation. The report is completed with a discussion, conclusions and recommendations for further research.

Chapter 2

Boom clay characterisation

2.1 Introduction

A selection of reference literature related to the characterisation of the Boom clay is provided. A description of the geology near the Oosterweel (Antwerp) area is given. The Boom clay stratigraphy is presented and used for a geomechanical subdivision. Subsequently the mineralogy, fractures and loading history are addressed. An overview of geotechnical parameters on the Boom clay and a brief explanation of characteristic clay strength and stiffness behaviour are also presented. This chapter concludes with a summary.

2.2 Geology

2.2.1 Stratigraphy

The Boom clay or Boom Formation (Bm) originated in the Late Tertiary period during the early Oligocene epoch, also sometimes known in Belgium as the Rupelian. The early Oligocene extended from 34 to 28 million years (Ma) ago and is part of the Middle Oligocene series (Vandenberghe [41], Jacobs et al. [19]). In the Antwerp area the Boom clay is between 60 and 80 metres thick . It dips 1-2 % towards the north-east and thickens in that direction. The base and thickness of the Boom clay in Belgium are displayed in Figure 2.1.

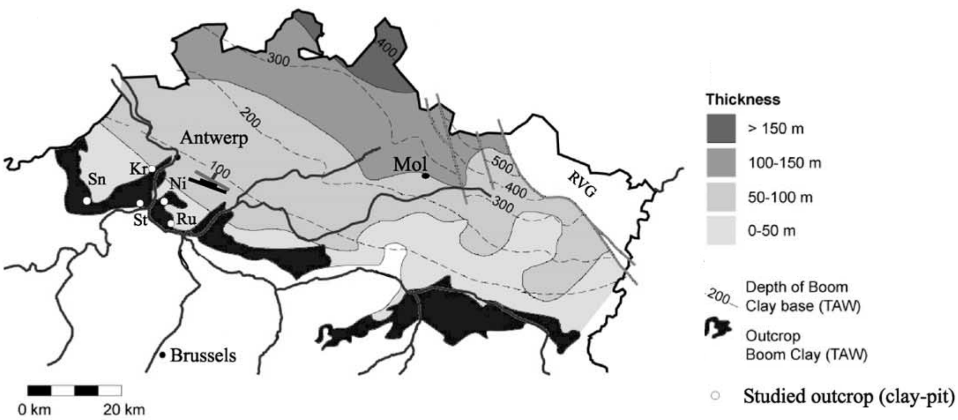

Figure 2.1: Base and thickness of Boom clay. Dehandschutter et al. [9].

Dehandschutter et al. [9] studied open clay-pits to determine the structure and composition of the Boom clay. The stratigraphy, the soil subdivision based on its time of deposition, near Oosterweel is shown in Table 2.1. Quartary formations and Neocene sands are present on top of the Boom clay. The Quartary and Neocene formations will not be further considered, since the focus is on the Boom clay. An elaborate lithostratigraphy, subdivison based on grain sizes and organic/carbonate content of these formations is given by Vandenberghe [41] and Jacobs et al. [19].

Period	Epoch	Formation	Denotation	Soil
Quartary	Holocene	Filler Sands	A	Silt
	Holocene	Alluvial clay	Q	Sand
	Holocene	Alluvial clay (peat)	Qp	Peat
Tertiary - Neogene	Pliocene	Lillo	Li	Sand
	Pliocene	Kattendijk	Kd	Sand
	Miocene	Berchem	Bc	Sand
Teriary - Paleogene	Oligocene	Boom clay	Bm0	Clay
	Oligocene	Boom clay	Bm	Clay

Table 2.1: Stratigraphy in the Oosterweel area. After Jacobs et al. [19] and RoTS [40].

The Boom Formation is divided into three members, the first one mentioned is closest to the surface:

Denotation	Member	Thickness (m)	Soil
BmPu	Putte	max. 45	Dark grey clay with organic bands
BmTe	Terhagen	20	Grey clay, low silt content
BmBw	Belsele-Waas	10	Grey silty clay

Table 2.2: Boom Formation (Bm) lithostratigraphical members. Jacobs et al. [19].

The Boom Formation contains silty bands with a high pyrite and glauconite content. In the Putte member septaria, bread-shaped carbonate concretions with a maximum height of 0.3 metre and diameter of 1 metre, were found and described by Schittekat et al. [36] and Jacobs et al. [19]. Fissures have also been observed in the Putte member. Schittekat et al. [36] suggest carefully selecting values for the top part of the Boom clay due to these septaria and fissures. The BmPu and BmBw members are siltier than the BmTe member, because of the adjacent (on top of and below the Boom clay) sand layers.

At the Oosterweel trial excavation cone penetration tests (CPTs) with a depth of 50 metres, to circa -45 TAW, have been performed for RoTS [40] ('Rechter oever Tunnel Specialisten', a tender company founded by Witteveen+Bos and Grontmij specifically for the Oosterweel project). TAW is the acronym for 'Tweede Algemene Waterpassing', which is the reference level in Belgium. Figure 2.2 shows a part of the resulting stratigraphy near the trial excavation area, indicated by the blue line. The denotations mentioned in the legend are stratigraphical subdivisions of the formations detailed in Table 2.1.

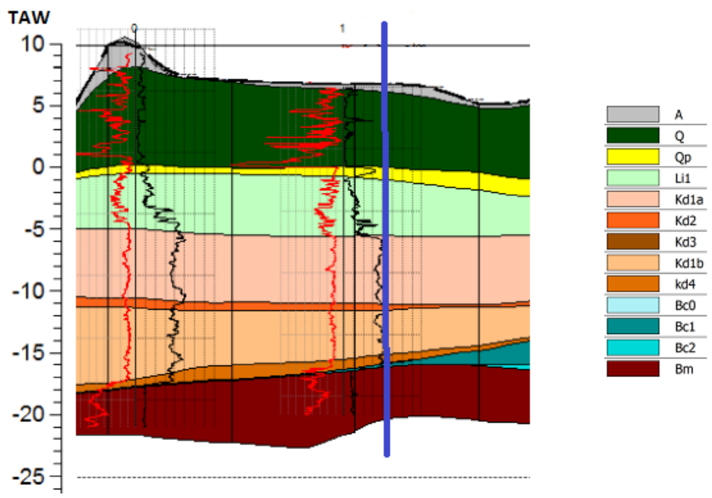

Figure 2.2: Stratigraphy near the Oosterweel trial excavation. After RoTS [40].

In the trial excavation the top of the Boom Clay is located at -17.3 m TAW and the bottom at approximately -80 m TAW. The stratigraphy displayed in Figure 2.2 is in accordance with the subdivisions provided by Jacobs et al. [19], Dehandschutter et al. [9], Schittekat et al. [36] and NIRAS [29].

2.2.2 Geomechanical subdivision

Schittekat et al. [36] propose dividing the Boom clay layer into five categories, based on extensive in situ and laboratory testing:

- BK0: A weathered top layer with thickness varying from a few decimetres to a maximum of 4 metres. It is light-coloured compared to other layers and there is some degradation in the geomechanical properties.
- BK1: A complex unit with a banded sequence mainly of silty and clayey horizons (horizontal bands), approximately 13 metres deep.
- BK2: A 15-metre thick layer, more clayey than BK1.
- BK3: A 30-metre thick black and grey clay layer. Revealing the presence of silty and clayey horizons.
- BK4: The bottom 10 metres of the Boom clay; it gradually grades into the underlying sands.

The orientation of the geomechanical BK layers is shown in Figure 2.3. The location of the Oosterweel trial excavation is shown by the blue line.

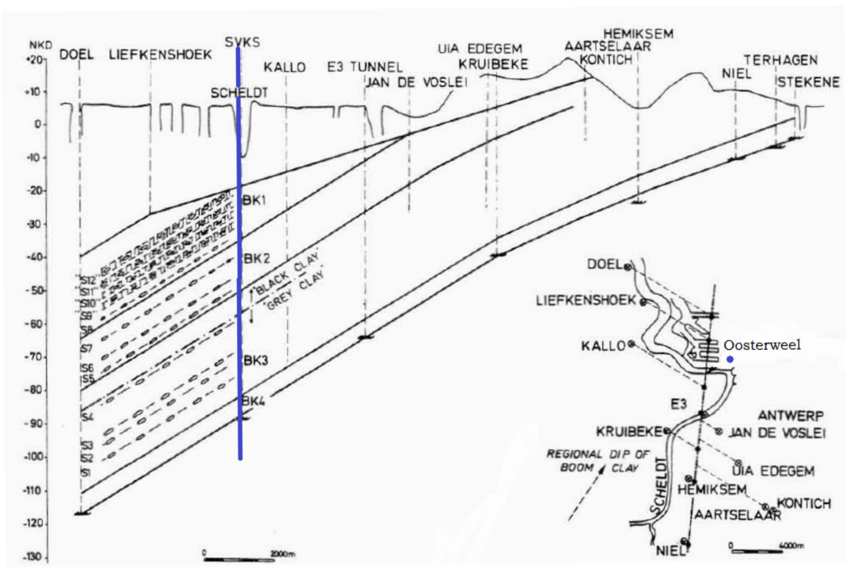

Figure 2.3: North-south cross section with BK layers. After Schittekat et al. [36]

The geomechanical subdivision is compared to the geological stratigraphy. This is useful when comparing reference literature using different notations for possibly the same layers. A comparison between the categorisations of the Oosterweel trial excavation is shown in Table 2.3 om page 6. This is an approximation, since the exact boundaries are not known. It should be viewed as a schematic visualisation of the stratigraphy of the Oosterweel trial excavation.

The bottom of the Oosterweel trial excavation lies at -17.3 m TAW and the sheet piles are at -25 m TAW. The influence of the layers below -50 m TAW on the trial excavation is negligible. This means that the BmPu or BK0, BK1 and BK2 layers are most relevant ones. The in situ measurements and laboratory tests performed by RoTS [40], that are discussed in the next chapter, are all performed on samples from the BmPu or BK0-2 layers.

Depth (m TAW)	Geological	Geomechanical
-18	BmPu	BK0
-20		BK0, BK1
-25		BK1
-30		
-35		BK1
-40		BK2
-45		
-50	BmPu	BK2
-55	BmTe	BK3
-60		
-65		
-70	BmTe	
-75	BmBw	BK3
-80	BmBw	BK4

Table 2.3: Schematic stratigraphy of the Oosterweel trial excavation. After Jacobs et al. [19] and Schittekat et al. [36].

2.2.3 Mineralogy

The mineralogy of the Boom clay is mainly dominated by clay minerals, quartz and feldspars. The values reported by various authors are similar, though relatively large variations in feldspar and Calcite content were found by Decleer et al. [8] and Honty & de Craen [18]. The main components of the Boom clay mineralogy are given in Table 2.4.

Mineral	Range (%)
Clay	
Kaolinite	1.0 - 15
Illite	3.0 - 30
Smectite	10 - 42
Non clay	
Quartz	24 - 58
Albite	3.2 - 6.2
K-feldspar	0.0 - 17
Calcite	0.0 - 4.3
Pyrite	0.2 - 8.9

Table 2.4: Minerals of the Boom clay. After Decleer et al. [8], Honty & de Craen [18] and NIRAS [29].

2.2.4 Fractures

Dehandschutter et al. [9] have studied the Boom clay in relation to the fractures on macro (joints) and micro (slickensides) scales. In Figure 2.4, scanning electron microscope (SEM) images of a Boom clay sample from the Kruibeke outcrop (Figure 2.1) are shown.

Both macro and micro fractures were also reported by Beerten et al. [2] and Schittekat et al. [36]. The macro fractures are found at depths of 40 - 50 metres in the Boom clay (Mertens et al. [27]). The micro fractures derived from consolidation related to volume reduction and uplift of the layer. They are observed to be randomly distributed over the outcropping parts of the Boom clay. Micro fractures are found in both weathered and freshly excavated zones, excluding artificial alteration as their origin (Dehandschutter et al. [9]). Schittekat et al. [36]

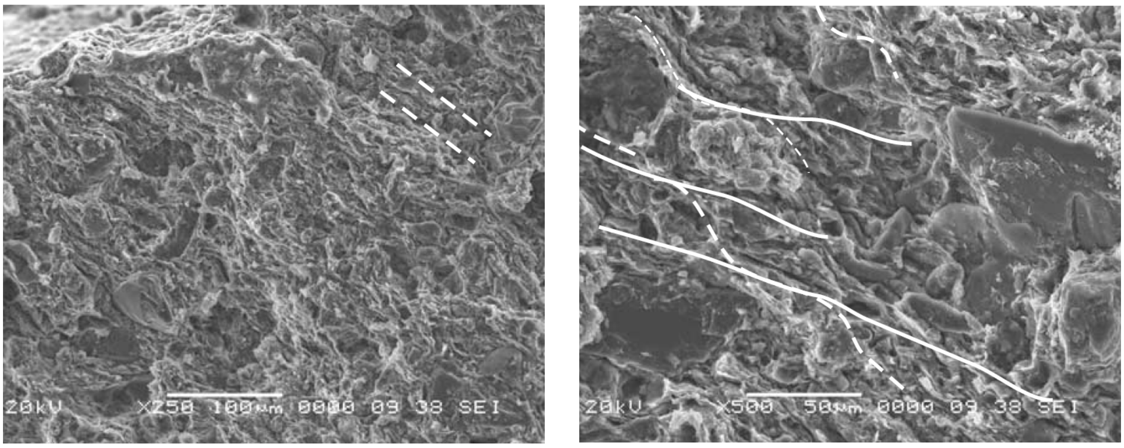

(a) Particle rotation. **(b)** Shear band development.

Figure 2.4: SEM images of a Boom clay sample, bedding is indicated with the dashed lines. Dehandschutter et al. [9].

suggest that these micro fractures originated at a compaction stage where the clay approached the lower plasticity condition.

2.2.5 Pre-loading and overconsolidation

The original thickness of the Boom clay was more than 100 metres, based on the 150 - 200 metre thick layer just north of the Belgian border. Schittekat et al. [35] [36] and Beerten et al. [2] state that 90 to 100 metres of the Boom clay layer has eroded to its current thickness of 69 - 72 metres at Oosterweel.
Based on geological derivations and laboratory tests, oedometers and self boring pressure meters (SBPMs), the removed overburden is determined to be 80 to 90 metres (Beerten et al. [2], Schittekat et al. [36]). The historical load is referred to as the 'past burial depth'. This characterises the Boom clay as an overconsolidated (OC) clay. At the top of the BmPu or BK0 layer current overburden is a maximum of 30 metres at Oosteweel, which is less than the historical 100 metres.
The quantity of overconsolidation is expressed with the overconsolidation ratio (OCR) or pre-overburden pressure (POP):

$$OCR = \frac{\sigma'_p}{\sigma'_v} \qquad\qquad POP = |\sigma'_p - \sigma'_v| \tag{2.1}$$

Where σ'_p is the largest historical vertical effective stress reached, the preconsolidation stress and σ'_v the in situ vertical effective stress. A soil is overconsolidated when σ'_p is larger than σ'_v, an OCR larger than 1.

The initial thickness of the Boom clay is estimated to be between 150 - 200 metres, with an assumed average of 175 metres (Beerten et al. [2], Schittekat et al. [36]). This implies that there is an approximate past burial depth of: $175 - 70 = 105$ metres clay. The vertical effective stress from this past burial, σ'_p, is calculated with Equation 2.2:

$$\sigma'_p = (\gamma_{sat}^{BC} - \gamma_w) \times d \tag{2.2}$$

with the saturated unit weight of the Boom clay, $\gamma_{sat}^{BC} = 20$ kN/m^3, the unit weight of water, γ_w $= 10$ kN/m^3 and the thickness of the eroded layer $d = 105$ m. Using these values in Equation (2.2) results in a presconsolidation stress of 1050 kPa.

The top of the Boom clay layer is covered by 26 metres of soil, predominantly sands at Oosterweel, as can be seen in Figure 2.2. The reference water level is at 4 m TAW (RoTS [40]). The in situ vertical effective stress at the top of the Boom clay is calculated with Equation 2.3:

$$\sigma'_v = (\gamma^S_{sat} - \gamma_w) \times d_{sat} + \gamma^S_{unsat} \times d_{unsat} \tag{2.3}$$

with the saturated unit weight of these sands, γ^S_{sat}, determined at 20 kN/m^3, γ^S_{unsat}, the sand's unsaturated unit weight equal to 17 kN/m^3, the thickness of the saturated sand, $d_{sat} = 22$ m and the thickness of the unsaturated sand, $d_{unsat} = 4$ m. This provides an in situ vertical effective stress of:

$$\sigma'_v = (20 - 10) \times 22 + 17 \times 4 = 288 \text{ kPa} \tag{2.4}$$

This leads to values for the OCR and a POP at the top of the Boom clay of:

$$OCR = \frac{1050}{288} \approx 3.6 \qquad POP = |1050 - 288| = 762 \text{ kPa} \tag{2.5}$$

2.3 Geotechnical parameters

2.3.1 Boom clay properties

In Table 2.5 the soil properties from previous research are given. The ranges are determined on Boom clay samples taken from a maximum depth of -80 m TAW.

Soil property	Symbol	Unit	Range
Saturated unit weight	γ_{sat}	kN/m^3	17.9 - 20.8
Unsaturated unit weight	γ_{unsat}	kN/m^3	14.6 - 16.5
Water content	w	%	22.0 - 30.0
Particle content < 2 μm	–	%	44.0 - 62.0
Porosity	n	%	35.0 - 41.2
Liquid limit	LL	%	60.0 - 80.0
Plastic limit	PL	%	23.6 - 25.0
Plasticity index	PI	%	40.0 - 53.1

Table 2.5: Range of Boom clay properties near the surface. After Dehandschutter [9], Schittekat [36], Schokking & van der Kolff [37] and RoTS [40].

Schokking & van der Kolff [37] and Schittekat et al. [36] present several properties per BK layer based on research performed near Antwerp and Mol. The properties for each BK layer are listed in Table 2.6.

Some differences between the BK layers were given, but no further depth trend is reported by the authors. Schokking & van der Kolff [37] observe uniformity in the Boom clay properties over large areas, ranging from Antwerp to the south of the Netherlands. They suggest that the geological history after consolidation has a limited effect on the geotechnical properties.

2.3.2 Strength Parameters

The shear strength behaviour shown by OC clay deviates from normally consolidated (NC) clay. This is shown in Figure 2.5. The removal of (overburden) pressure increases the water content, but that increase is much smaller than the decrease of water content during consolidation.

The clay at point (b) is under the same effective pressure as point at (d), but has a higher water content. This means that the packing of the particles at (d) is denser, thus resulting in higher shear strength (Skempton [39]).

Soil property	Unit	BK0*	BK1	BK2	BK3
γ_{sat}	kN/m^3	19.0 - 20.0	19.4 - 20.0	19.2 - 20.0	19.3 - 20.0
$< 2\mu m$	%	44	50 - 54	57 - 62	50 - 54
w	%	22	23 - 27	24 - 29	22 - 30
LL	%	71	66 - 80	73 - 81	60 - 77
PI	%	47	40 - 52	44 - 53	35 - 51

Table 2.6: Range of Boom clay properties per BK layer. After Schittekat et al. [36] and Schokking & van der Kolff [37]. *Average value as opposed to range.

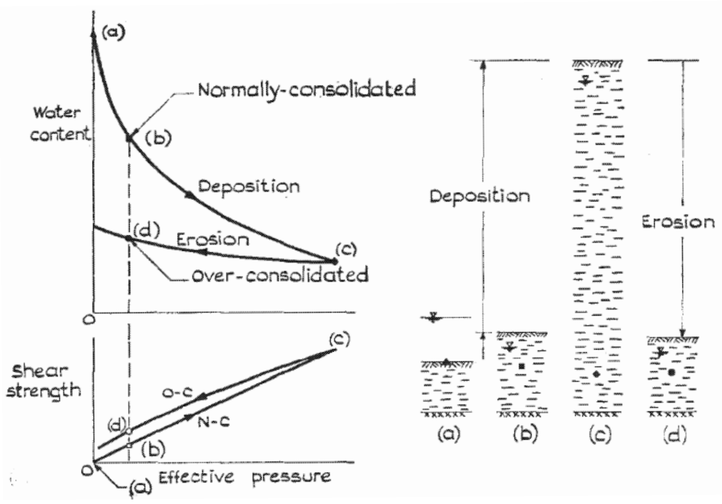

Figure 2.5: Differences in OC and NC clay strength with visualisation of burial depth. Skempton [39].

2.3.2.1 Effective stress

The effective soil strength is described by the parameters, c' the effective cohesion and φ' the angle of internal friction. The effective soil parameters are often determined with triaxial (TA) or direct simple shear (DSS) tests. The Coulomb equation is used to determine the peak shear strength, s_f:

$$s_f = c' + \sigma' \times tan\varphi' \tag{2.6}$$

This represents the peak shear resistance a soil can offer. This peak shear strength, s_f is commonly referred to as the 'shear strength'. When multiple tests are performed at different effective pressures, the Coulomb equation (2.6) can be displayed in a shear strength versus effective pressure plot. Figure 2.6 shows this for an OC clay in a drained shear box test. If the test is continued beyond s_f, the strength decreases while the displacement increases, this process is known as strain softening [39]. The shear strength does not decrease to zero but will reach the residual (shear) strength, s_r. The residual strength also satisfies the Coulomb equation, where s_f, c' and φ' are replaced by the residual values s_r, c'_r and φ'_r. Figure 2.6 displays a very small residual cohesion (intersection dashed line and vertical axis), which is often the case with OC clays.

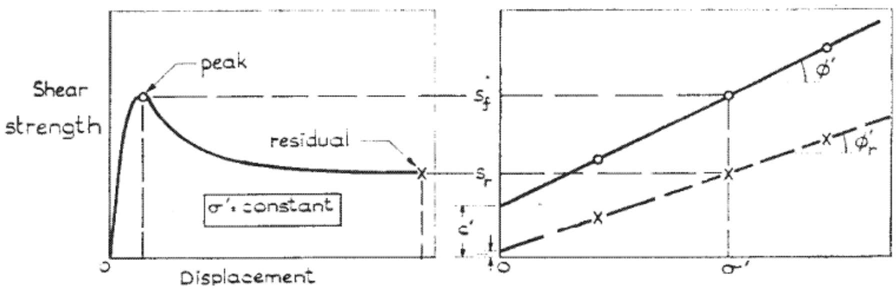

Figure 2.6: Shear strength versus displacement and σ'_v for OC clay in drained shear box tests. Skempton [39].

Peak values are more commonly reported in literature. A summary of the Boom clay's peak effective strength parameters is given in Table 2.7.

Parameter	Symbol	Unit	Range
Peak effective friction angle	φ'	^{o}	17.1 - 25.0
Peak effective cohesion	c'	kPa	15.0 - 48.0

Table 2.7: Peak effective strength parameters for the Boom clay. After de Beer [7], Schittekat [36], MOW [28] and RoTS [40].

Skempton [39] states that the strength parameters of fractures and joints in OC clays will lie close to the residual value. De Beer [7] has determined residual strength parameters for the Boom clay near Antwerp. He reports the following residual values; $\varphi'_r = 11 - 22^o$ and $c'_r = 0$ kPa.

2.3.2.2 Total stress

Soil behaviour in terms of total stress is characterised with the undrained shear strength, s_u. This is used for the response shortly after loading of soils with low permeability. The s_u is not one value for OC clay, but a function of σ'_v and the OCR. This relationship was found by Ladd & Foot [24], and is known as the Stress History And Normalised Soil Engineering Properties (SHANSEP) equation:

$$s_u = \sigma'_v \times S \times (OCR)^m \tag{2.7}$$

With S, the normally consolidated ratio of s_u, ranging from 0.2 - 0.3 and m, an empirical exponent often between 0.7 and 1.0. Instead of listing ranges of s_u values functions are given in Table 2.8.

Method	Function
de Beer [7]	$s_u = 75 + 3.5z$
Schittekat [36]	$s_u = 175 + 0.8z$
Ladd & Foot [24]*	$s_u = \sigma'_v \times 0.3 \times (OCR)^{0.8}$

Table 2.8: Undrained shear strength Boom clay. *Based on other OC clays.

The thickness of the clay layer, z in metres results in s_u values in kPa for the first two equations in Table 2.8. The s_u from the SHANSEP equation has the same unit as the corresponding σ'_v. This equation is often used and frequently validated for OC soils (Ladd & de Groot [23]). The exact determination of S and m is not always straightforward. Ladd & de Groot [23] present the lower and upper boundaries for S and m, derived from the different types laboratory tests. TA compression tests generally form the upper and TA extension tests the lower boundary, with DSS tests in between them.

2.3.3 Stiffness Parameters

Brinch Hansen & Mise [5] investigated incremental loading (IL) oedometer tests on OC Little belt clay. Samples were loaded up to 3 MPa, then unloaded and reloaded. This resulted in the characteristic 'bilinear' curves in a log σ' - ε plane, shown in Figure 2.7 (a).

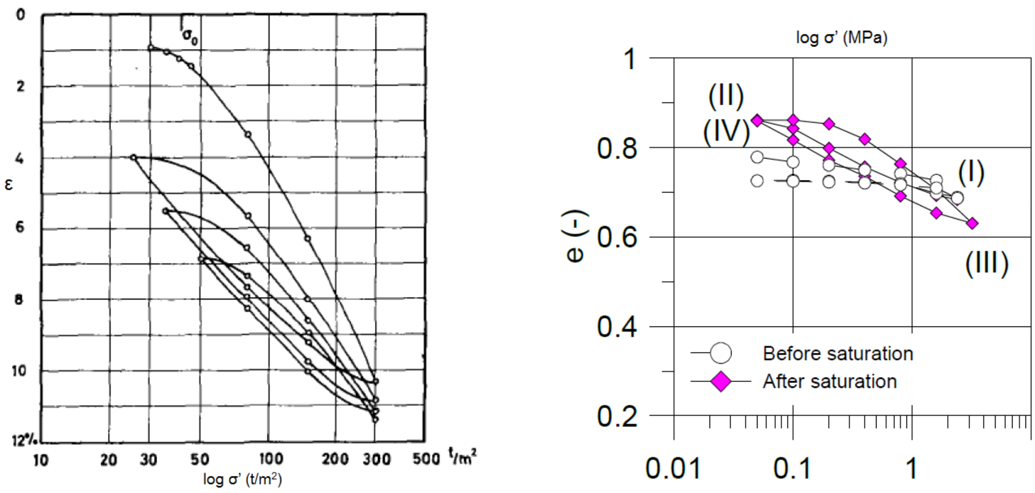

(a) Little Belt clay. **(b)** Boom clay.

Figure 2.7: Bilinear curves after unloading and reloading of OC clay in IL oedometer test. After (a) Brinch Hansen & Mise [5] and (b) Deng et al. [11].

Deng et al. [11] performed IL oedometer tests on the Boom clay in a similar stress range, from 0.05 to 3.2 MPa, displayed in Figure 2.7 (b). Please note that the plot in (a) displays *log* σ' versus ε where (b) shows *log* σ' versus e. These results display similar behaviour in constrained unloading/reloading.

Brinch Hansen & Mise [5] derived the following equations to describe this relationship:

$$\varepsilon_u = \varepsilon_{u;0} - b_u \left(log \frac{\sigma'_u}{\sigma'} \right)^n, \quad \varepsilon_r = \varepsilon_{r;0} + a_r \left(log \frac{\sigma'}{\sigma'_r} \right)^m \text{ and } \; b_u = a_r \left(log \frac{\sigma'_u}{\sigma'_r} \right)^{m-n} \tag{2.8}$$

They propose distinguishing between the unloading strain, ε_u and the reloading strain, ε_r. The incremental strain is determined with respect to the initial strain at the beginning of unloading and reloading, $\varepsilon_{u;0}$ and $\varepsilon_{r;0}$. The effective stress at the beginning of unloading an reloading are indicated with σ'_u and σ'_r respectively. Finally the coefficients b_u, a_r depend on the empirical coefficients m and n. The Equations (2.8) were used by de Beer [7] for his calculations on the Boom clay. Ladd & de Groot [23] emphasise the importance of the virgin compression ratio, CR:

$$CR = \frac{C_c}{1 + e_0} \tag{2.9}$$

with C_c, the compression index and e_0, the initial void ratio of the soil. The recompression ratio, RR is often approximated at a fifth of the CR (Ladd & de Groot [23]). The bilinear curves in Figure 2.7 indicate a lower RR, at the beginning of unloading. When settlements over time are considered the rate of secondary compression, C_α can be relevant. This rate is defined as:

$$C_\alpha = \frac{\Delta \varepsilon_v}{\Delta log\ t} \tag{2.10}$$

with $\Delta\varepsilon_v$, the incremental vertical strain and $\Delta log\ t$ the logarithmic time increment.

2.3.4 Permeability

Extensive research on the permeability of the Boom clay is performed on samples taken at Mol, from a depth of approximately -200 m TAW. Other samples were gathered for the Western Scheldt tunnel in the Netherlands, where the Boom clay is around 25 metres from the surface (Rijkers et al. [33]). These samples are taken from the same BmPu formation or BK0-1 layer, which is at -20 m TAW at Oosterweel. The coefficient of horizontal permeability, k_h is approximately twice the coefficient of vertical permeability, k_v (Marivoet et al. [25]). Ranges for the horizontal and vertical permeability of the Boom clay are given in Table 2.9. The large range of the permeability coefficients can be attributed to the difference in sample depth.

Parameter	Symbol	Unit	Range
Coefficient of vertical permeability	k_v	m/s	$1.3 \times 10^{-12} - 1.5 \times 10^{-9}$
Coefficient of horizontal permeability	k_h	m/s	$3.5 \times 10^{-12} - 5.8 \times 10^{-8}$

Table 2.9: Permeability parameters Boom clay. After Deng et al. [10] [11], Marivoet et al. [25], and Rijkers et al. [33].

2.3.5 Swelling

A characteristic property of the Boom clay and OC clays in general is its potential to swell or expand. Two swelling processes are distinguished:

- Free swelling on hydration.
- Swelling due to stress relief.

Swelling on hydration applies to unsaturated soils which become saturated, leading to a volume expansion. A soil which has previously been loaded and is unloaded will swell due to the stress relief. Swelling on hydration is often correlated to the classification parameters.

Gromko [14] states that three components are necessary for potentially damaging hydration induced swelling to occur:

1. The natural water content must be around the plastic limit.
2. A water source for the heave must be present.
3. The soil contains montmorillonite, a family of very soft phylosillicate clay minerals.

Correlations between a soil's degree of expansion and the classification parameters are shown in Table 2.10.

Degree of expansion	PI (%)	LL (%)
Very high	> 35	> 70
High	25 - 41	50 - 70
Medium	15 - 28	35 - 50
Low	< 18	20 - 35

Table 2.10: Degree of expansion ranges correlated to classification data. After Holtz [17] and Kalantari [21].

For the construction of the Deurganckdock lock near Antwerp a very large excavation to the top of the Boom clay was made. That excavation is 68 metres wide, 500 metres long and 30 metres deep, resulting in a large stress relief for the Boom clay (Vinke et al. [42]). The initial or primary swelling, directly after excavation, was not monitored due to construction difficulties. The measuring equipment was installed from the bottom of the building pit, after the excavation. Vinke et al. [42] reported a swelling rate of 2 mm per month in the first months after excavation. They also mention a heave of the access road to the Kennedy tunnel (Antwerp) of 1 to 1.5 mm per year to date. The Boom clay is still swelling there, even though this road was constructed over 40 years ago.

Femern, a tender company created for the Ferhmarnlink tunnel between Germany and Denmark, investigated the OC Paleogene clay in the Baltic sea. This Paleogene clay has a high plasticity and is heavily OC. It is folded and contains shear bands from its geological history, especially from glacial actions. A large scale trial excavation was performed close to the German coast in the Baltic sea to monitor this clay in an excavation. An area of 30 by 70 metres was excavated, with a depth of 10 metres from the seabed. A total heave of 37 millimetres with respect to the bottom of the excavation was measuered after nine months (Femern [13]). Femern considers the swelling process as reversed consolidation, distinguishing the primary swelling as a result of pore pressure changes and the secondary swelling resembling (reversed) creep. This method is initiated by Femern and is not general practice. They designed this approach to numerically describe the swelling process of Paleogene clay. The primary swelling is approximated using the (1D) Terzaghi equation:

$$\frac{\delta u}{\delta t} = \frac{E_{oed}}{\gamma_w}\frac{\delta}{\delta z}\left(k\frac{\delta u}{\delta z}\right) \tag{2.11}$$

where the E_{oed} is expressed as a function of σ'_v and k is a function of the void ratio. Femern stated that the heave measured in the first nine months was most likely driven by permeability and not by the soil stiffness. They also state that secondary heave can be significant and is in the order of approximately 30 - 50 % of the primary heave. The effect of the secondary swelling is modelled with Equation (2.12):

$$\varepsilon_{sw} = c_{sw} \times log\ \left(1 + \frac{t}{t_b}\right) \tag{2.12}$$

with ε_{sw} the strain due to secondary heave, c_{sw} the rate of secondary swelling and t_b a reference time. Based on the 1D heave model Femern predicts a primary heave of 160 to 280 millimetres and secondary heave of 80 - 100 millimetres, 120 years after the excavation (Femern [13]).

2.4 Summary

The Boom clay is an overconsildated Paleogene clay, with a thickness of approximately 70 at Oosterweel. Geologically it is divided in the Putte, Terhagen and Belsele-Waas member, comparable to a subdivision in BK0-2, BK3 and BK4 layers. The Boom clay contains fractures on both micro and macro scale. It has been subjected by a past burial depth of over 100 metres, resulting in its overconsolidated state.
Classification, stiffness and strength parameters are listed. The strength behaviour of OC clay is shown, with shear strength generally higher than NC clay. Parameters for effective strength are given. The undrained shear strength should be seen as a function of depth or of σ'_v and the OCR. Oedometer tests with characteristic 'bilinear' stress strain relationship are presented, displaying that the Boom clay has a lower RR at the start of unloading. Furthermore coefficients of permeability are listed. Finally the swelling behaviour is addressed and heave measurements on similar Paleogene clays are given.

Chapter 3

Geotechnical parameters from laboratory tests

3.1 Introduction

This chapter covers the parameter determination from the performed laboratory tests on the Boom clay. Over one hundred Boom clay samples were gathered from depths of -21.1 m TAW to -37.6 m TAW. Classification, strength, stiffness, permeability and consolidation parameters will be given.

3.2 Classification

Classification parameters are important to determine the consistency of fine grained soils. The soil consistency can be correlated to soil behaviour. The classification parameters were derived from 24 Boom clay samples. The determined Atterberg values are plotted versus depth in Figure 3.1.

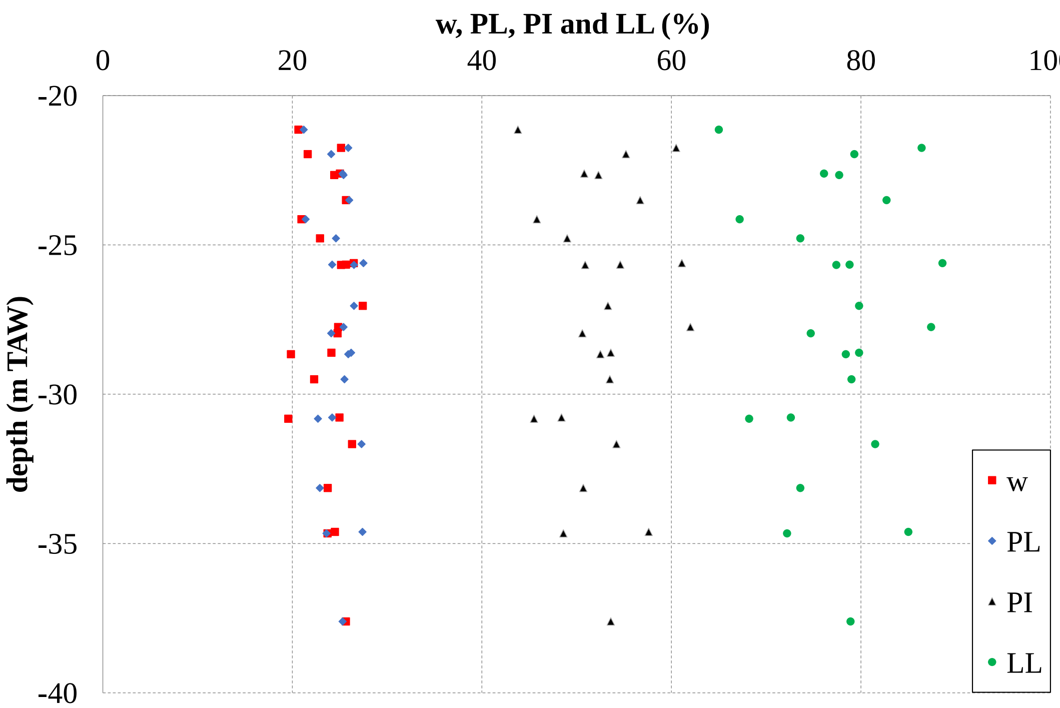

Figure 3.1: Classification parameters versus depth.

The plasticity index, PI and liquidity index, LI are calculated as:

$$PI = LL - PL \qquad LI = \frac{w - PL}{PI} \tag{3.1}$$

Figure 3.1 displays almost constant values over depth, no clear depth trend can be determined. The minimum, maximum and and average values of all samples are displayed in Table 3.1.

Property	w	LL	PL	PI	LI	γ_{sat}	γ_{unsat}	e
Unit	%	%	%	%	-	kN/m^3	kN/m^3	-
Minimum	19.6	65.0	21.2	43.8	-0.115	19.8	15.6	0.562
Maximum	27.4	88.6	27.5	62.0	0.027	20.5	17.0	0.697
Average	24.0	77.7	25.0	52.7	-0.019	20.1	16.2	0.634

Table 3.1: Minimum, maximum and average values of classification parameters

The ranges are similar to the values from the reference literature. It is observed that the natural water content is very close to, even below, the plastic limit. This indicates a dense and stiff clay, from which water has been extruded due to the preconsolidation stress. For the calculations the average values are used.

3.3 Strength

In this section the effective and undrained strength parameters are discussed. The effective parameters are derived from the TA compression and extension tests. The undrained shear strength is derived from the TA compression tests and compared to the SHANSEP equation.

3.3.1 Effective strength

From the TA tests the c' and φ' values are determined. These are peak values, determined at maximum deviatoric stress (failure). Figures 3.2 and 3.3 display the result in a $s' - t$ plane, where $s' = (\sigma_1' + \sigma_3')/2$ and $t = (\sigma_1' - \sigma_3')/2$.

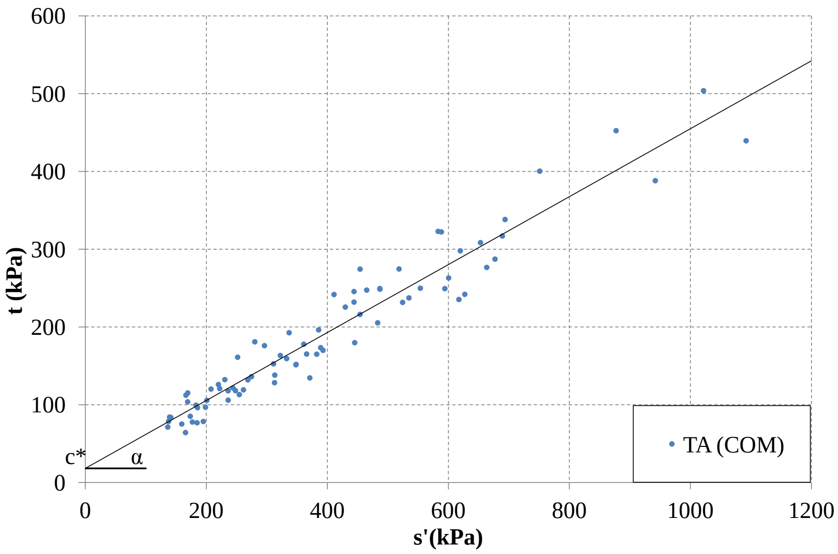

Figure 3.2: TA compression tests performed on Boom clay samples with best fit line for peak values.

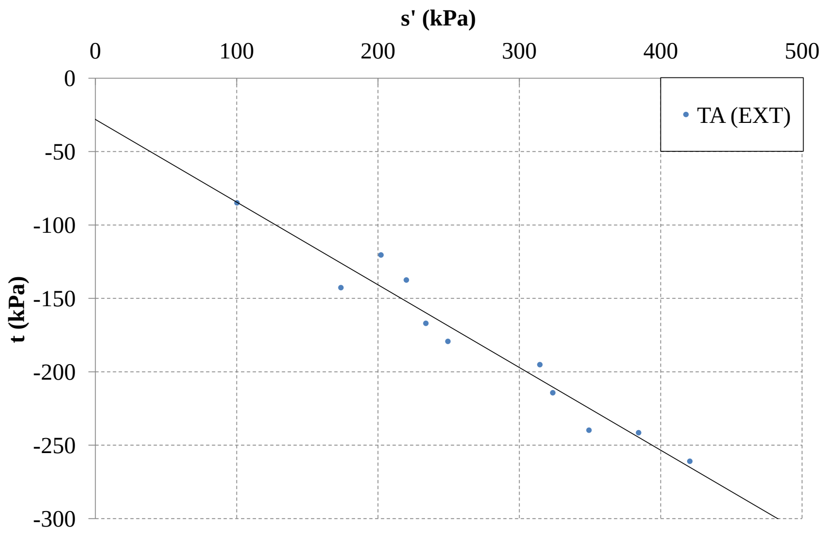

Figure 3.3: TA extension tests performed on Boom clay samples with best fit line for peak values.

The angle of the black line and the horizontal axis in Figure 3.2 is defined as α. The φ' is derived using Mohr-Coulomb and the gradient of this trend line:

$$\varphi' = arcsin(tan\ \alpha) \tag{3.2}$$

The intersection of this line with the t-axis provides c^*, this is used to determine the effective cohesion:

$$c' = \frac{c^*}{cos\ \varphi'} \tag{3.3}$$

Using the above mentioned equations with Figures 3.2 and 3.3 results in the strength parameters given in Table 3.2.

	Unit	Compression	Extension
φ'	^{o}	25.9	34.4
c'	kPa	20.2	33.9

Table 3.2: Peak effective strength values from TA tests.

It is worth noting that the extension tests provide higher values than the compression tests. This is remarkable, especially since the difference is significant. There is no straightforward explanation for this deviation. There were less extension tests performed than compression tests, but the trend seems to be consistent over the available samples. The compression values are used in the calculations.

3.3.2 Undrained shear strength

The undrained strength of Boom clay is dependent of the vertical effective stress and the OCR. This is combined in the SHANSEP equation for OC clays. This equation can be used with the values derived from the from the TA tests. Figure 3.4 shows TA data and the fit with the SHANSEP equation.

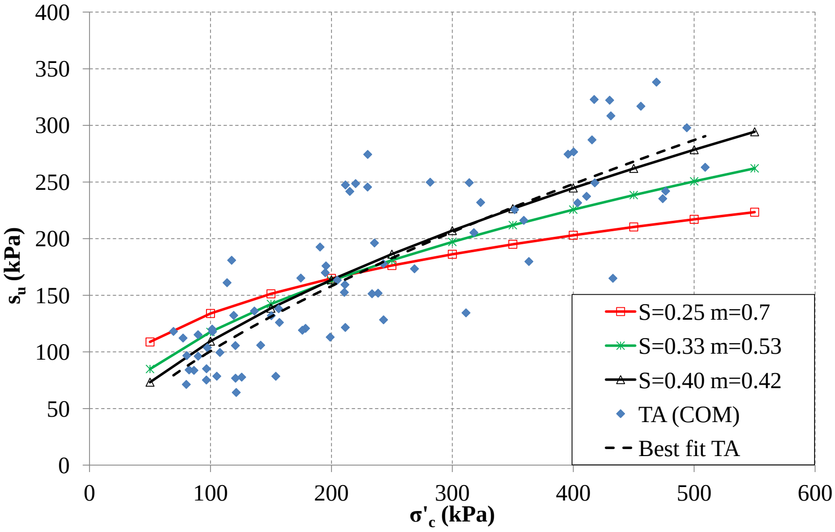

Figure 3.4: The undrained shear strength from the TA tests (blue scatter) with best fit (dashed) line. SHANSEP approximations given by red, green and black lines.

From the reference literature it is determined that the σ'_v at the top of the Boom clay is approximately 300 kPa with a σ'_p of 1050 kPa. The in situ stresses are compared to the results from the triaxial tests by taking $\sigma'_v = \sigma'_c$. The effect of the preconsolidation can then be expressed using the following relations:

$$OCR = \frac{\sigma'_p}{\sigma'_c} \qquad POP = |\sigma'_p - \sigma'_c| \tag{3.4}$$

The POP is visualised in Figure 3.5. It assumes that the influence of the σ'_p is the same at each stress level.

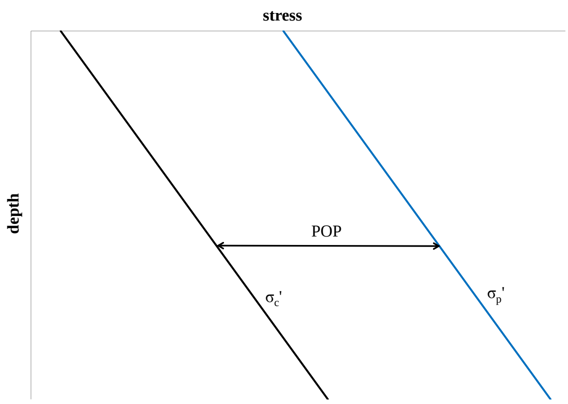

Figure 3.5: The effective consolidation pressure (blue), preconsolidation pressure (black) and POP over depth.

To compare these values to the SHANSEP equation the OCR needs to be calculated. Under these assumptions the best fit for the SHANSEP equation is:

$$s_u = \sigma'_c \times 0.40 \times (OCR)^{0.42} \tag{3.5}$$

Ranges found under the mentioned assumptions do not match the values from literature. A possible explanation might be that the effect of the preconsolidation is not conserved in the current state. The best fit is found with $S = 0.40$ and m is 0.42. This is a higher S and lower

m than the values reported by Ladd $ de Groot [23], who specify a ranges for $S = 0.2 - 0.3$ and for $m = 0.7 - 1.0$.

3.4 Stiffness

Stiffness parameters can be determined from multiple laboratory tests. The laboratory tests discussed in this section are IL oedometer tests and isotropic CU triaxial tests. There were 23 oedometer tests performed with unloading and reloading steps. A total of 41 triaxial tests have been performed, of which 27 compression tests, with 13 tests containing unloading and reloading steps. The other 14 triaxial tests are extension tests.

3.4.1 Stiffness from oedometer tests

When determining stiffness parameters from oedometer tests on OC clay it is important to determine the preconsolidation stress, σ'_p. Casagrande already explained in 1932 that soil has a 'memory' for stress change and that these changes are stored in the soil structure. The σ'_p can be derived from oedometer tests when loaded to a stress beyond the σ'_p. For the top of the Boom clay the σ'_p is determined from the reference literature (Schittekat et al. [36]), at 1050 kPa.

From the 23 oedometers tests all but one were loaded up to a maximum of 1000 kPa. The other oedometer test was loaded up to 1977 kPa. To determine the CR a test loaded to a minimum of four times the σ'_p is needed, to ensure that the sample is in the virgin compression range (Ladd & de Groot [23]). This would mean an oedometer test to over 4 MPa for the Boom clay. In absence of such a test the one loaded to 1977 kPa was used to determine the CR. This is visualised in Figure 3.6, where the CR is shown by the red line.

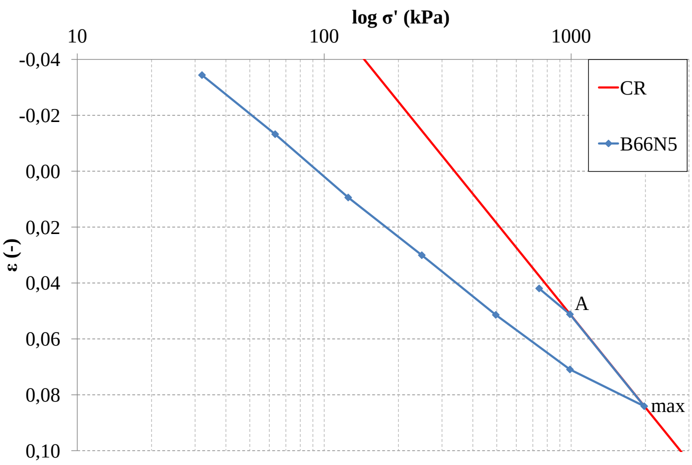

Figure 3.6: The IL oedometer loaded to the highest stress on Boom clay sample B66N5 (blue) and the CR line (red).

The CR is determined from the tests shown in Figure 3.6 with:

$$CR = \frac{\Delta\varepsilon}{log(\sigma'_{max}/\sigma'_A)} \tag{3.6}$$

where σ'_{max} is the maximum effective stress on the sample, and σ'_A the largest available effective stress before the maximum stress. This results in the following value for the CR:

$$CR = \frac{0.084 - 0.051}{log(1977/989)} \approx 0.11 \tag{3.7}$$

Deng et al. [11] have performed oedometer tests on Boom clay samples that were loaded to more than 30 MPa, far beyond the σ'_p. They reported a CR of circa 0.20, determined from a range of 4 to 20 MPa. For the calculations a CR of 0.11 is used. This value is a low estimate for the Boom clay's CR, it is the CR close to the σ'_p.

The recompression ratio can also be determined with Equation (3.6), when the strain increment and stress range are covering unloading-reloading part. Figure 3.7 shows the $log\ \sigma' - \varepsilon$ plot for one sample. The blue curve representing the data from the oedometer test starts at a relatively high stress, around 370 kPa. The sample is loaded stepwise up to this stress, but the next loading step is immediately applied if the sample is still expanding. The values before this stress are not given, since the interval between the loading steps was not the same as for the other steps. This procedure is chosen in order to minimise sample disturbance due to swelling, resulting in a sample closest to the in situ conditions. Therefore the blue line in Figure 3.7 shows only two loading steps, followed by five unloading steps.

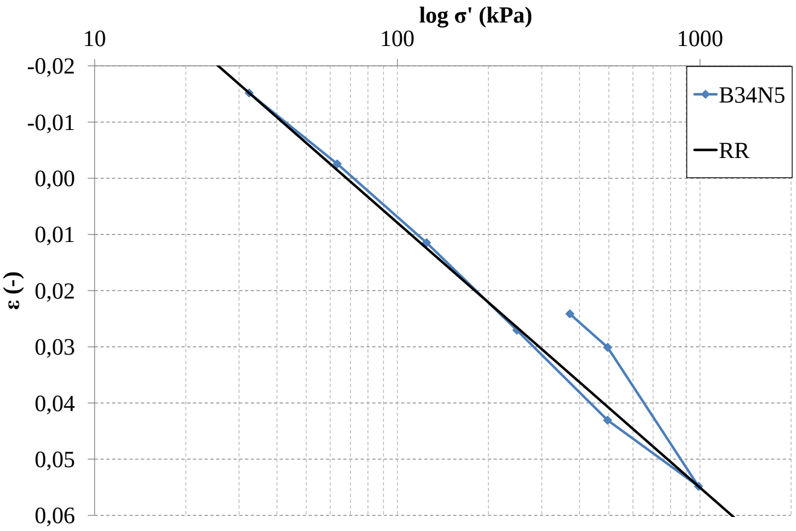

Figure 3.7: An IL oedometer test on Boom clay sample B34N5 (blue) and the RR (black).

The determined recompression ratio, shown by the black line in Figure 3.7, is based on the entire unloading stress range. For the line Figure 3.7 this results in:

$$RR = \frac{0.055 - -0.015}{log(988/32)} \approx 0.047 \tag{3.8}$$

This RR value is lower than the one determined from the stress step at the beginning of unloading. The full unloading stress range is chosen since this is representative for an excavation, where almost all vertical stress on the Boom clay will be released. For the 22 oedometer tests RR values have been determined. An average value of $RR = 0.042$ has been derived.

3.4.2 Stiffness from triaxal tests

The 13 isotropically consolidated undrained compression triaxial tests will be referred to as compression TA tests for convenience in this section. The major principal effective stress is denoted with σ'_1. The lateral effective stresses are σ'_2 and σ'_3, here under triaxial conditions; $\sigma'_2 = \sigma'_3$.

An example of a series of TA compression test is given in Figure 3.8. Sample (c) was performed under the highest σ'_c of 359 kPa. The other samples were performed at 50%, (b) and

25%, (a) of this σ'_c. Figure 3.8 displays the a resulting $\varepsilon_1 - q$ plot, with ε_1 the vertical strain and the deviatoric stress, $q = \sigma'_1 - \sigma'_3$ under triaxial conditions.

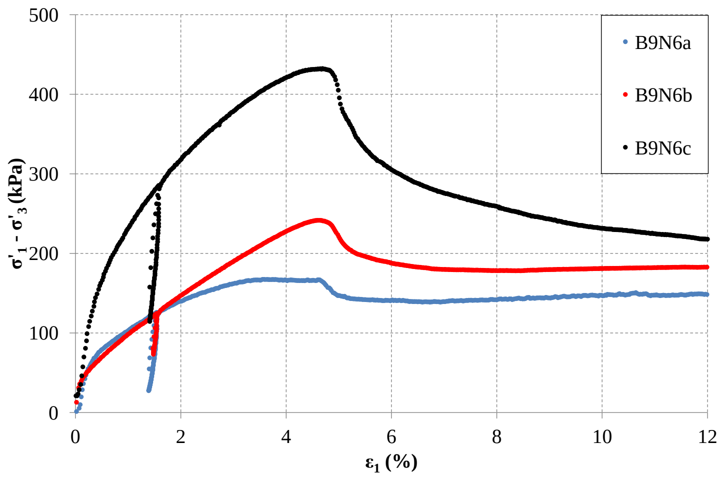

Figure 3.8: Triaxial tests with unloading and reloading steps of Boom clay samples B9N6a-c at three confining pressures.

These unloading and reloading steps are seen from the drop and recovery of q between 1.5% ε_1 and 2% ε_1. The associated stress paths are shown in Figure 3.9 in a $s' - t$ plane.

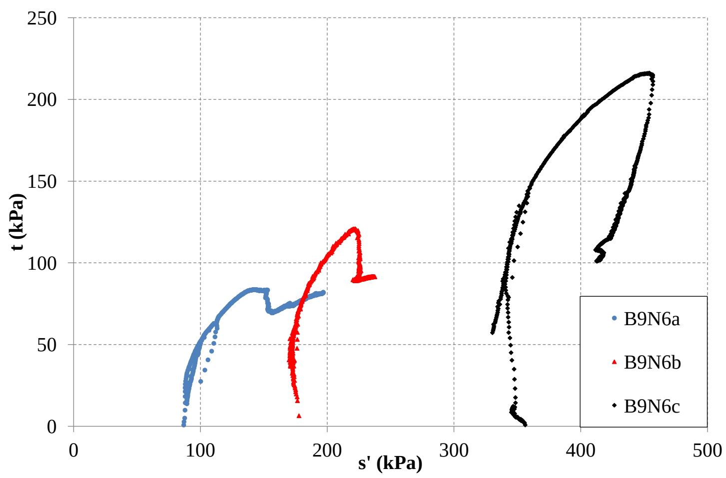

Figure 3.9: Effective stress paths for samples B9N6a-c.

From the tangent and secant lines several commonly used stiffness moduli can be determined. The maximum deviatoric stress at failure, q_f, is used for the determination of the stress range for these stiffness. These E moduli are:

- E_i, the initial stiffness. This is determined with the slope of the tangent line at the start of the loading. Preferably in the curve's linear part in the $\varepsilon_1 - q$ plot, with maximum range of $q = 0$ to $q = q_f/3$ or $\varepsilon_1 = 0\%$ to $\varepsilon_1 = 0.1\%$.
- E_{50}, the stiffness at 50 % of the q_f. The slope of the secant line from the origin and the curve point $(\varepsilon_1, q_f/2)$.
- E_{ur}, the stiffness in unloading - reloading. Approximated with the slope of the secant line from the start of the deviatoric unloading and the beginning of reloading.

The lines representing the E_i, E_{50}, E_{ur} are shown in Figure 3.10 on page 22. These values are best determined with linear regression on the available data points. Since soil stiffness is stress dependent, these E moduli are considered with the consolidation stress level.

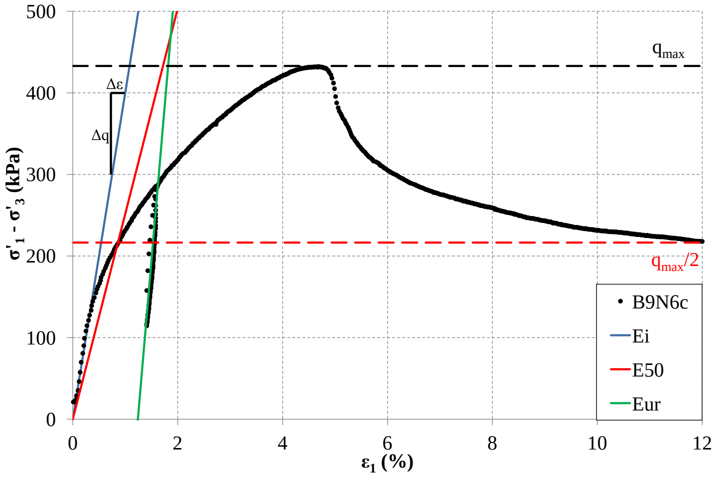

Figure 3.10: Triaxial test of Boom clay sample B9N6c with the coloured lines used to determine E moduli. The E_i is derived from the blue line, E_{50} from the red line and E_{ur} from the green line.

The E moduli are determined with:

$$E = \frac{\Delta q}{\Delta \varepsilon} \tag{3.9}$$

This results in the following values:

$$E_i = \frac{123}{0.038} = 32.3 \text{ MPa} \qquad E_{50} = \frac{217}{0.086} = 25.2 \text{ MPa} \qquad E_{ur} = \frac{171}{0.0018} = 95.0 \text{ MPa} \tag{3.10}$$

These E moduli are related to one stress level. When comparing values from multiple tests at different stresses it is useful to relate them to a reference stress level, which is the same for all used values. These reference values will be derived in the next chapter.

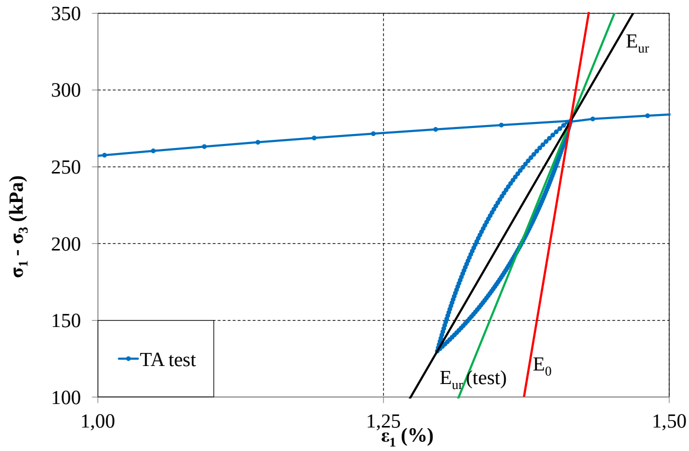

Figure 3.11: Zoom on unloading-reloading loop in TA test (blue). Visualisation of difference between E_0 (red) and theoretical value of E_{ur} (black) and E_{ur} from the laboratory tests (green).

The E_{ur} appears to be a relatively high value. This can be caused be the fact that the unloading steps also measure the initial stiffness, E_0. So the initial stiffness is measured rather than the E_{ur}, Figure 3.11 illustrates this.

The E_0 influences the beginning of the unloading part, where at larger strains the elastic unloading reloading is reached. If the unloading-reloading loop covers a larger strain range the influence of E_0 is less significant. When only a smaller strain range is covered, as is the case in many of the laboratory TA tests, the influence of E_0 should be taken into account. Then the E_{ur} is be much closer to the E_0 than the 'theoretical' value of E_{ur}. Therefore E_{ur} should be reduced with approximately a factor 2: $\frac{1}{2}\Delta q$, which results in an $E_{ur} = 47.5$ MPa for the test displayed in Figure 3.10.

When determining small strain stiffness often the initial shear modulus, $G_0 = E_0/(2(1+\nu_{ur}))$ is used. For the determination of G_0 Atkinson & Sällfors [1] defined three shear strain ranges; very small, small and large as shown in Figure 3.12. The initial elastic soil stiffness is constant in the very small strain range, below $\gamma \approx 1 \times 10^{-3}\%$. Under undrained triaxial conditions $\gamma = \frac{3}{2}\varepsilon_1$.

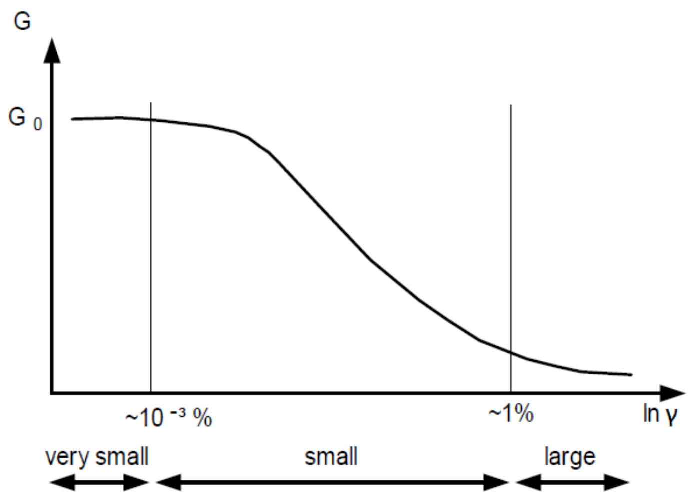

Figure 3.12: Idealised variation of stiffness with strain. From Piriyakul [30] after Atkinson and Sällfors [1].

The stiffness decreases with an increase of γ, which is illustrated by a characteristic 'S-curve'. Conventional triaxial tests are not able to determine shear strains smaller than circa 0.01 %. However the data for the unloading reloading steps from the TA tests were close to the very small strain range. This can imply that influence of the initial stiffness is measured in the unloading reloading steps.

The performed TA tests were all undrained, as is often the case with clays. The derived E moduli are therefore also undrained and should be referred to as E^u values. Ideally one would like the drained values to determine the properties of a soil, this is however difficult for soils with low permeability. Drained E values are can be calculated from E^u with:

$$E = E^u \times \frac{1+\nu}{1+\nu_u} \tag{3.11}$$

where E is the drained stiffness modulus, ν Poisson's ratio and ν_u the undrained Poisson's ratio with a value of approximately 0.5.

3.5 Consolidation and permeability coefficients

From 12 of the IL oedometer tests the coefficient of consolidation, c_v and the coefficient of permeability, k are determined. These tests were all performed with unloading and reloading steps. The c_v is determined with the Casagrande *log t*-method. The values of c_v and k for sample B9N5 are presented in Figure 3.13.

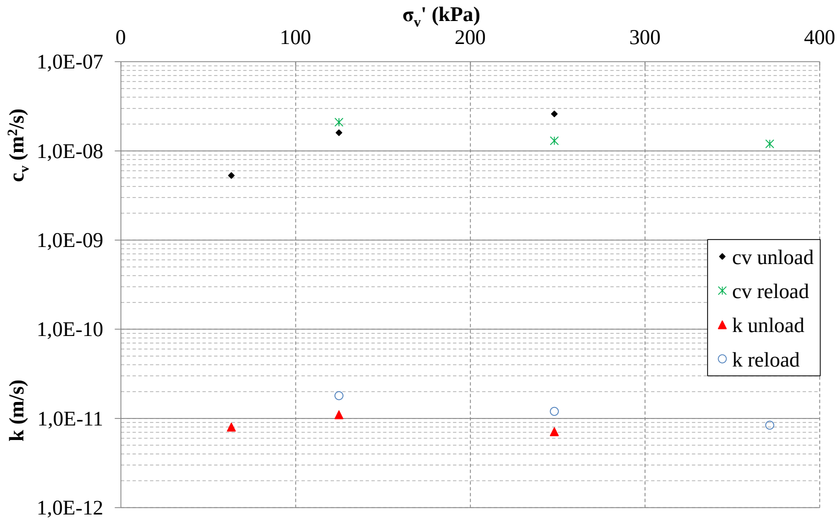

Figure 3.13: Consolidation and permeability coefficients from IL oedometer test on sample B9N5.

The c_v and k values were reported for unloading and reloading separately, to identify a possible difference between them. The coefficients derived for all IL oedometer tests are visualised in Figure 3.14.

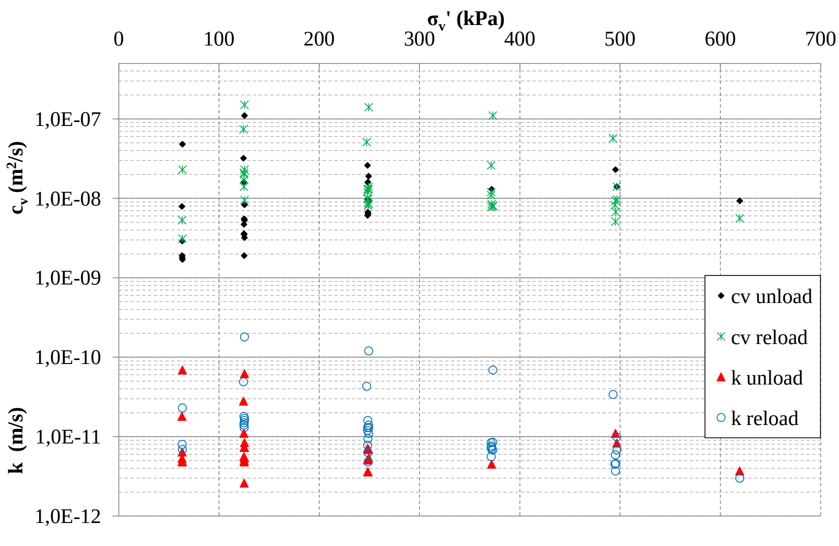

Figure 3.14: Consolidation and permeability coefficients in unloading and reloading from the IL oedometer tests.

The resulting values are given in Table 3.3.

	c_v (m^2/s)	k (m/s)
Minimum	1.7×10^{-9}	2.6×10^{-12}
Maximum	4.5×10^{-7}	1.8×10^{-10}
Average	3.1×10^{-8}	2.0×10^{-11}

Table 3.3: Ranges of c_v and k.

Figure 3.14 displays that the c_v and k values in unloading are slightly below the reloading values. This is however not sufficient to conclude that they are significantly different, since some scatter is present. The average c_v and k values are used in the calculations.

$$E_{oed} = \frac{c_v}{k} \times \gamma_w \tag{3.12}$$

Equation (3.12) displays the relationship between these coefficients and the oedometer stiffness. Checking this for the average values results in an E_{oed} of:

$$E_{oed} = \frac{3.1 \times\ 10^{-8}}{2.0 \times\ 10^{-11}} \times 10 \approx 15.5 \text{ MPa} \tag{3.13}$$

The value of 15.5 MPa is relatively high, but is in the correct order of magnitude. It is slightly over half the E_i. Further determination of these parameters will be discussed in the next chapter.
These permeability coefficients are derived on laboratory scale and it is known that these are generally lower than the in situ conditions. This can be related to the existence of fractures on macro scale, which are not captured in a homogeneous laboratory sample. These k values are therefore considered as a lower boundary for the coefficient of permeability.

3.6 Summary

In this chapter the parameters derived from the performed laboratory tests on Boom clay samples were presented. The average values are summarised in Table 3.4:

w	γ_{sat}	γ_{unsat}	e	CR	RR	φ'	c'	c_v	k
%	kN/m^3	kN/m^3	-	-	-	^{o}	kPa	m^2/s	m/s
24.0	20.1	16.2	0.634	0.11	0.042	25.9	20.2	3.1×10^{-8}	2.0×10^{-11}

Table 3.4: Summary of average values of parameters from laboratory tests

These values will be used for the calculations on the trial excavation. The stress and strain dependent E moduli and s_u are not mentioned in this summary, since they require further analysis before they can be used in the calculations.

Chapter 4

Numerical model

4.1 Introduction

In this chapter the steps taken for the numerical calculation of the trial excavation are explained. Firstly the choice for the material models is argued, with a concise explanation of the selected models. Secondly the derivation for the required parameters is given. Thirdly the numerical approximation of the trial excavation in Plaxis is illustrated. This chapter concludes with a summary and an overview of the model parameters.

4.2 Material Models

A concise description of the relevant material models will be discussed in this section. For a more elaborate explanation of the models it is advised to consult Benz [3], Schanz et al. [34] or the Plaxis material models manual [31].

4.2.1 Material model selection

The selection of a suitable material model is crucial for a numerical calculation. The selection is often dependent on the available (laboratory) data for the required parameters. There is no merit in using a complex model when little is known on the input parameters. For the numerical calculation on the trial excavation extensive laboratory work is available. Numerous material models are available and it is considered beyond the scope of this research to elaborate on all of them. Instead the choice of the selected models is motivated.

The Hardening Soil with small strain stiffness (HSs) is the best standard model in Plaxis for an excavation (Brinkgreve [6]). It is one of few models that is able model OC soil and unloading situations. A known limitation is that the HSs model tends to overestimate deformations in an excavation. An adaptation of the HSs, the generalised hardeing soil (GHS) model is developed to deal with this limitation, as well as using all features of the HSs. The influence of small strain stiffness is to be considered, the HSs is currently the only (standard) model that incorporates this. Therefore the HSs and GHS model are used. This section will further expand on these material models.

4.2.2 Hardening soil with small strain stiffness

The Hardening Soil with small strain stiffness (HSs) model is an expansion of the Hardening Soil (HS) model. The HS model is based on the hyperbolic relationship between the vertical strain and deviatoric stress in primary triaxial loading. Kondner & Zelasko [22] were the first to describe this relationship for drained triaxial tests on sand with the following equation:

$$\varepsilon_1 = \frac{1}{2E_{50}} \frac{q}{1 - q/q_a} \quad \text{for } q < q_f \quad \text{and } q_a = \frac{q_f}{R_f} \tag{4.1}$$

where q_a is the asymptotic value of deviatoric stress and q_f the deviatoric stress at failure. This asymptotic value is related to deviatoric stress at failure with the ratio R_f. Since the asymptotic stress is always higher than value at failure R_f is smaller than 1. The q_f is derived from the Mohr-Coulomb failure criterion:

$$\begin{aligned}(\sigma_1-\sigma_3) &= 2c\,cos\varphi+(\sigma_1+\sigma_3)sin\varphi\\ q_f &= 2c\,cos\varphi+q_f\,sin\varphi+2\sigma_3\,sin\varphi\\ q_f(1-sin\varphi) &= (c\,cot\varphi+\sigma_3)2\,sin\varphi\\ q_f &= (c\,cot\varphi+\sigma_3)\frac{2sin\varphi}{1-sin\varphi}\end{aligned} \tag{4.2}$$

The effective cohesion and effective friction angle are indicated with φ and c instead of φ' and c' for convenience. The stiffness modulus E_{50} is determined with the secant stiffness at $q_f/2$. The stress dependency of this modulus is given by:

$$E_{50}=E_{50}^{ref}\left(\frac{A+\sigma_3'}{A+p_{ref}}\right)^m \qquad \text{with } A=c'\times cot\varphi' \tag{4.3}$$

with p_{ref} the reference stress level, the minor principal stress, σ_3' and E_{50}^{ref} the stiffness modulus at the reference stress [31]. The m value represents the magnitude of stress dependency of the stiffness. Typical m values are 0.5 for sands (Janbu, [20]) and 1 for soft clays, since this simulates the logarithmic compression behaviour.

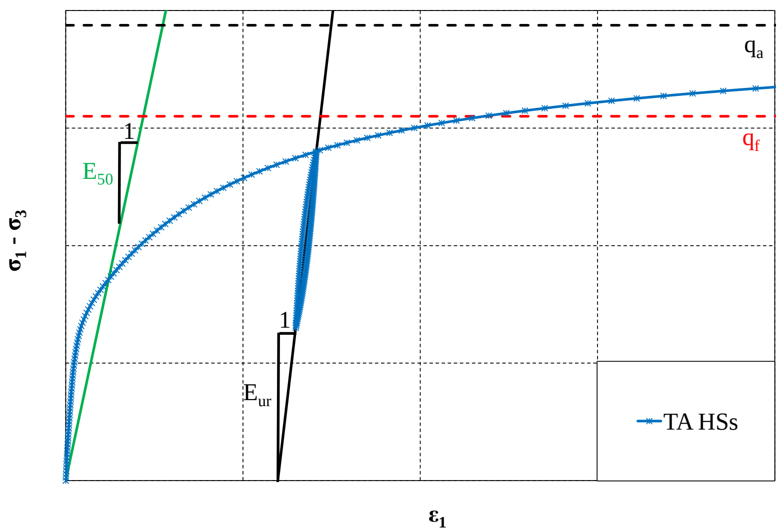

Figure 4.1: Triaxial test with lines used to determine E_{50} (green), E_{ur} (black). The q_a and q_f are given by the dashed black and red line.

The relationship given in Equation (4.3) is also used for the E_{ur}, which is determined from unloading/reloading steps.

$$E_{ur}=E_{ur}^{ref}\left(\frac{A+\sigma_3'}{A+p_{ref}}\right)^m \tag{4.4}$$

These E moduli are visualised in in Figure 4.1. The oedometer stiffness follows in a similar fashion:

$$E_{oed}=E_{oed}^{ref}\left(\frac{A+\sigma_3'/K_0^{nc}}{A+p_{ref}}\right)^m \tag{4.5}$$

The E_{oed} is derived from one-dimensional compression tests, where the vertical effective stress σ_1' is varied. This results in the term of σ_3'/K_0^{nc}, which is equal to σ_1' in primary one dimensional compression. The HS model incorporates both friction and compaction hardening.

The Plaxis material models manual [31] offers a more elaborate description of this model and an explanation of the implemented constitutive equations. It should also be mentioned that the HSs does not incorporate softening or time dependency.

The previous E moduli do not account for the strain dependency of stiffness, soil displays a higher stiffness at smaller strains. This is characterised within the HSs model with the initial shear modulus, G_0 (Plaxis [31]). This G_0 is mobilised in the very small strain range, for strains smaller than 1×10^{-3}%. It decreases with increasing shear strain, a formulation for this decrease with respect to the secant shear modulus G_s is given by Hardin & Drnevich [15]. When a shear strain at which the G_s is reduced to circa 70% of its initial value, the $\gamma_{0.7}$ is used in the Hardin & Drnevich equation (dos Santos & Correia [12]), this leads to:

$$\frac{G_s}{G_0} = \frac{1}{1 + 0.385\ |\gamma/\gamma_{0.7}|} \tag{4.6}$$

Equation (4.6) results in a strong stiffness reduction when γ becomes much larger than $\gamma_{0.7}$. At larger shear strains the small strain stiffness will reach the unloading/reloading shear modulus, G_{ur} which is calculated from the E_{ur} and ν_{ur}:

$$G_{ur} = \frac{E_{ur}}{2(1+\nu_{ur})} \tag{4.7}$$

The stiffness degradation curve with $\gamma_{0.7}$ and cut-off at G_{ur} are visualised in Figure 4.2.

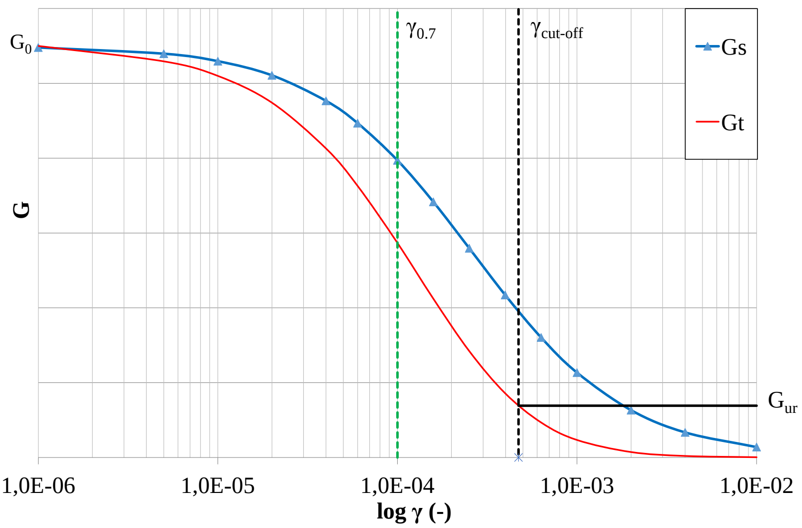

Figure 4.2: Small strain stiffness reduction in terms of secant (blue) and tangent (red) shear modulus as a function of shear strain, with $\gamma_{0.7}$ (dashed green) and $\gamma_{cut-off}$ (dashed black).

The tangent shear modulus, G_t is obtained by taking the derivative with respect to γ of the G_s, resulting in

$$G_t = \frac{G_0}{(1+0.385(\gamma/\gamma_{0.7}))^2} \tag{4.8}$$

Equation (4.8) is bounded by a lower limit for larger (shear) strains. As is seen in Figure 4.2, reaching the G_{ur} value corresponds with a certain cut-off shear strain, $\gamma_{cut-off}$. This can be calculated with:

$$\gamma_{cut-off} = \frac{1}{0.385}\left(\sqrt{\frac{G_0}{G_{ur}}} - 1\right)\gamma_{0.7} \tag{4.9}$$

The calculated value of $\gamma_{cut-off}$ in (4.9) corresponds to the G_t and not to the G_s line. The stress dependency of G_0 follows the same power law as Equations (4.3) and (4.4):

$$G_0 = G_0^{ref} \left(\frac{A + \sigma_3'}{A + p_{ref}} \right)^m \tag{4.10}$$

The required material parameters for the HSs model are given in Table 4.1.

Symbol	Property	Unit
c'	Effective cohesion	kPa
φ'	Effective friction angle	$^\circ$
ψ	Dilatancy angle	$^\circ$
E_{50}	Secant stiffness for drained TA test	MPa
E_{oed}	Tangent oedometer stiffness primary loading	MPa
E_{ur}	Unloading/reloading stiffness	MPa
G_0	Inital shear modulus	MPa
$\gamma_{0.7}$	Shear strain at which $G_s = 0.722G_0$	-
m	Magnitude of stress dependency	-
p_{ref}	Reference stress level	kPa
ν_{ur}	Poisson's ratio for unloading/reloading	-
K_0^{nc}	K_0 value for normally consolidated state	-
R_f	Failure ratio q_f/q_a	-

Table 4.1: Parameters for the HSs model

Some of these parameters were directly derived from the laboratory tests. The derivation of all parameters will be discussed in the subsequent sections. All numerical values for these parameters are presented at the end of this chapter.

4.2.3 Generalised hardening soil

The GHS model is available as a user defined soil (UDS) model in Plaxis [32]. This model is developed to give a more accurate response for OC soils in excavations. Since the HSsmall model can predict an unrealistic reduction of stiffness with decreasing stress, though this reduction is not displayed in reality due to the effect of the effective preconsolidation stress. The GHS the effect of that stress on the stiffness moduli. Two new formulations for the power law of the stiffness moduli are introduced:

$$E = E^{ref} \left(\frac{(\sigma_p' + \sigma_3')/2}{p^{ref}} \right)^m \tag{4.11}$$

$$E = E^{ref} \left(\frac{(\sigma_p' + p')/2}{p^{ref}} \right)^m \tag{4.12}$$

The most significant difference between these equations and those of the HSs model, e.g. Equations (4.3) and (4.10), is the absence of strength parameters and input of preconsolidation stress. This power law is the same for all stiffness moduli: E_{ur}, E_{oed}, E_{50} and G_0, in agreement with the HSs model (Plaxis [32]). It should also be noted that the effective preconsolidation stress it not a constant value, but varies with depth. This model uses the same parameters as the HSs, displayed in Table 4.1, besides its extra options.

When the same reference moduli as in the HSs are used, the GHS will calculate a higher stiffness at low stress levels. To obtain comparable results in an excavation, the reference values for the GHS should be smaller than those for the HSs. Since $(\sigma_p' + \sigma_3')/2$ or $(\sigma_p' + p')/2$ will often be equal to or larger than $\sigma_3' + A$, with a large σ_p' and realistic material parameters.

The modular options for the GHS are summarised in Tables 4.2 and 4.3. These display the 'switches' for the stress and strain dependency and the plasticity model.

For the plasticity model the different yield functions of the HSs model are separately available. The minimum setting uses only the Mohr-Coulomb (MC) model and the full plasticity model includes all yield functions of the HSs.

Option	**Value**
MC model only	1
Shear hardening and MC	2
Cap harderning and MC	3
Shear & cap hardening and MC	4

Table 4.2: Plasticity model options for the GHS model

The stress dependent stiffness option with value 2 means that the E moduli are updated per calculation step, which is done by default in Plaxis. Alternatively a value of 0 can be chosen, equal to $m = 0$ in the HSs, which implies no stress dependency of stiffness. Another option is to update the stiffness per calculation phase, value 1. This can be useful in a dynamic calculation to avoid unwanted fluctuations in very small steps. This is not relevant for the calculation on the trial excavation and not used in the calculation. The strain dependency option specifies whether small strain stiffness is included. This is either on, value 1 or off, value 0. For the stress dependency formula three options are available. Value 0 results in the original HSs formula, value 1 in Equation (4.11) and value 2 in Equation (4.12) on page 30. Since the HSs model is already considered separately option 1 and 2 are used within the GHS.

This results in the values given in 4.3, which are used for the calculations with the GHS model.

Option	**Value**
Stress dependent stiffness	2
Strain dependent stiffness	1
Plasticity model	4
Stress dependency formula	1 or 2

Table 4.3: Modular options for the GHS model used in the calculation

4.3 Determination of model parameters

This section addresses the derivation of the numerical parameters. Beginning with the strength parameters and some deviating choices with respect to default values in Plaxis 2D. Then the stiffness parameters are given, followed by the flow parameters.

4.3.1 General

4.3.1.1 Strength parameters

The strength and classification parameters from the previous chapter are used. The effective strength parameters can be used without further adjustment, using the Undrained(A) calculation option in Plaxis which is recommended for the HSs.

As is mentioned before, these parameters are peak average values. An argument can be made to also consider residual values. However it can be seen from the TA tests that the residual values become relevant at strains larger than circa 3 to 5% for the Boom clay. These ranges are rarely reached in the trial excavation and are therefore not considered. Another argument

	Unit	Value
c'	25.9	kPa
φ'	20.2	^{o}

Table 4.4: Strength parameters.

against reduction of the strength parameters is the favourable results from the TA extension tests. These are not used because only a limited number of extension tests were performed and they lacked unloading/reloading steps.

4.3.1.2 Preconsolidation

For the OCR and POP the values from the literature are used, resulting in an OCR = 3.6 or POP = 1050 kPa at the top of the Boom clay layer. Many soils have an unloading/reloading Poisson's ratio with a default value of 0.2 in Plaxis. Because of the OC state of the Boom clay it is chosen to deviate from this default value. This is based on the relation from Mayne & Kulhawy [26] regarding OC soil and the determination of the K_0:

$$K_0^{oc} = (1 - sin\varphi') \times OCR^{sin\varphi'} \tag{4.13}$$

The aim is to approach Equation (4.13) in Plaxis, assuming that this equation properly accounts for the influence of OC in unloading. To check this an oedometer test with an unloading step is simulated. Starting from the a stress state, comparable to the in situ conditions, the unloading path is displayed in 4.3 for different unloading/reloading Possion's ratio. The incremental change in stress coefficient (K) for unloading/reloading is given by:

$$\frac{\nu_{ur}}{1 - \nu_{ur}} \tag{4.14}$$

Figure 4.3 displays the effective vertical stress versus the effective horizontal stress, for unloading in an simulated oedometer test. The initial stress state at the beginning of unloading is given by $\sigma'_h = K_o^{nc} \times \sigma'_v = 168$ kPa. From Figure 4.3 it can be seen that a ν_{ur} of 0.3 better approaches the relationship given in (4.13), than a ν_{ur} of 0.2.

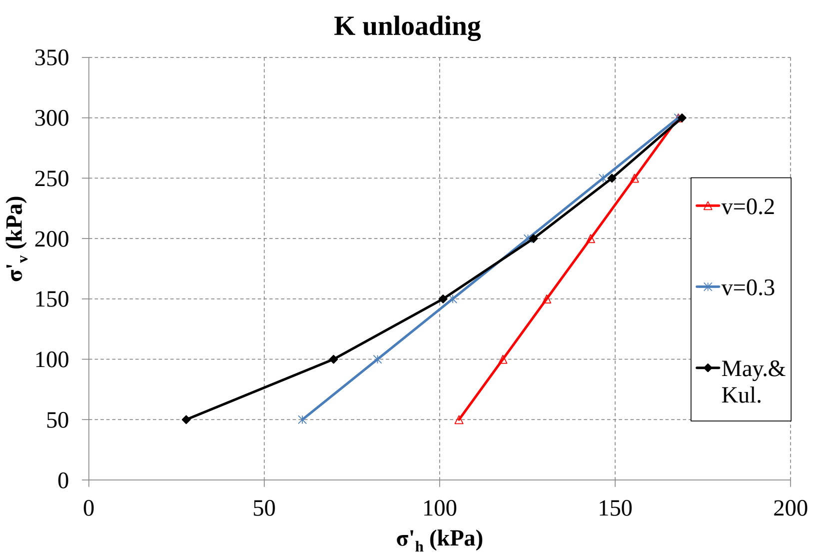

Figure 4.3: Relation of horizontal and vertical stresses as generated by Plaxis with Poisson's ratio 0.2 (red) and 0.3 (blue) and the theoretical value as determined from Mayne & Kulhawy (black).

4.3.1.3 Failure ratio

Another deviation from the default values is the choice for a R_f of 0.8 over 0.9. The SoilTest facility was used to simulate the TA test in Plaxis. This facility is based on a single point algorithm, allowing for a quick check for the material model and parameters compared to the laboratory test. It was found that the simulated failure occurred at larger strains than shown in the laboratory test, therefore it was decided to a reduce the R_f.

4.3.2 Stiffness parameters

4.3.2.1 E moduli

When numerically modelling an excavation, the E_{ur} is the most important stiffness modulus. This modulus determines the response in unloading. It is defined based on triaxial tests, but can also be determined from oedometer tests with unloading/reloading steps. The E_{ur} derived from an oedometer should be theoretically recalculated to an E_{ur} value. This is, assuming linear elastic behaviour, shown in Equation (4.15):

$$E_{ur} = E_{ur}^{\text{OED}} \frac{(1+\nu)(1-2\nu)}{(1-\nu)} \approx E_{ur}^{\text{OED}} \times 0.74 \tag{4.15}$$

for $\nu = 0.3$. Using the average RR value from the previous chapter and assuming $m = 1$, thus the $ln(10)$ term, the E_{ur}^{ref} from te oedometer tests can be determined as follows:

$$E_{ur}^{ref} = \frac{p^{ref}}{RR} \times ln(10) \times 0.74 \tag{4.16}$$

Using Equation (4.16) with a reference stress of 300 kPa results in an E_{ur}^{ref} from the oedometer tests of:

$$E_{ur}^{ref} = \frac{300}{0.042} \times ln(10) \times 0.74 \approx 12.2 \text{ MPa} \tag{4.17}$$

This value is based on oedometer tests only and would more accurately be referred to as E_{ur}^{ref}(OED). This distinction will not be made because this is not possible in the HSs model. One E_{ur}^{ref} value is required, since the E_{ur}^{ref} is defined based on the from unloading/reloading steps in a triaxial test. As is mentioned in the previous chapter half the deviatoric stress was used for this E modulus, because of the supposed influence of small strain stiffness. This is supported by (unrealistically) high values of the E_{ur} otherwise.

Because of the stress dependency of stiffness the determined E moduli are corrected for the σ'_c from the triaxial tests. This is done by plotting the determined E_{ur} against the σ'_c and fitting the HSs power law, see Figure 4.4 on page 34. Although some scatter is observed in this figure a value for m of 0.7 seems reasonable. Then the reference moduli can be determined with Equation (4.4), rewritten to:

$$E_{ur}^{ref} = E_{ur} \times \left(\frac{A + p_{ref}}{A + \sigma'_3} \right)^m \tag{4.18}$$

where σ'_3 is equal to σ'_c. For the performed TA tests a range of 18 to 47 MPa was found, with an average reference value ($p^{ref} = 300$ kPa) of 32 MPa.

This value can be viewed as a lower boundary, since the value of deviatoric stress in the unloading/reloading range was reduced by a factor two. This E_{ur}^{ref} is still more than twice as large as the one calculated in Equation (4.17). A possible explanation for this difference is given by the influence of the small strain stiffness. Since the strain ranges of the oedometer tests cover almost a full percent of strain, while the unloading reloading in the TA test is in a much smaller strain range. This deviation in E_{ur} can therefore be caused by the influence of the small strain stiffness shown in the TA tests and not in the oedometers. The parameters that account for the influence of small strain stiffness are addressed in the next section.

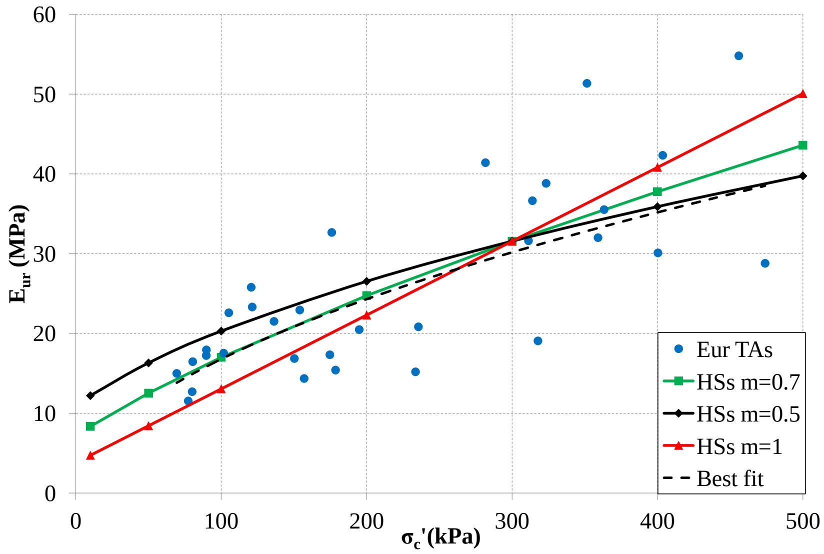

Figure 4.4: Determination of m value from triaxial tests.

4.3.2.2 Small strain stiffness

Figure 4.5 displays G_s moduli from TA tests performed with σ'_c ranging from 270 to 480 KPa.

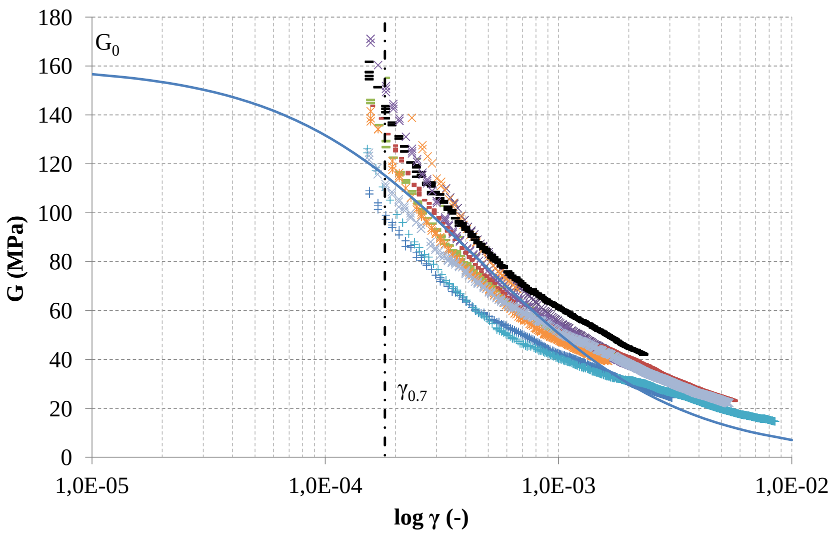

Figure 4.5: Secant shear moduli determined from unloading steps of triaxial tests (scattered lines), with best fit (blue) of S-curve and $\gamma_{0.7}$ (dashed) line.

There are no accurate measurements available from the very small strain range ($< 1 \times 10^{-3}\%$), however many points close to that range are available. The strong increase of G_s near very small shear strain range indicates the influence of small strain stiffness. The results from the TA tests were therefore used to determine the G_0 parameter. This is done by using the stiffness degradation curve, Equation (4.6), to estimate a G_0 value. The values in the larger shear strain ranges are used to fit the S-curve. With sufficient points from multiple tests a theoretical curve can be drawn, which results in a G_0 value.

To obtain the G_0^{ref} values there has to be accounted for the different cell pressures. The same m value of 0.7 is also chosen for this power law. This is partly done for practical reasons, since there is no option to specify an m value for G_0^{ref} deviating from the one for the other E moduli in the HSs. It is unclear if the stress dependency of small strain stiffness is different than that of the regular stiffness. In this calculation it is assumed this is not the case. As can be seen this results in a G_0 value of approximately 160 MPa. Using a similar procedure as for the E_{ur} the range for G_0^{ref} was determined at 100 to 180 MPa, with an average value of 150 MPa for a reference stress level of 300 kPa. It is remarked that this an approximation, but consistent among the numerous TA tests. In the calculations a relatively conservative value of $G_0 = 120$ MPa is used.

The $\gamma_{0.7}$ is also determined from Figure 4.5, simply by determining the value at 0.722 G_0. This resulted in a range for $\gamma_{0.7}$ of 1×10^{-4} to 3×10^{-4}. The $\gamma_{0.7}$ does not appear to display stress dependency, but is approximately the same value at different stress levels.

4.3.2.3 The E_{oed} and E_{50}

The other stiffness parameters for the HSs and GHS are the E_{oed} and E_{50}. The E_{oed} is determined relatively straightforward from the oedometer tests. Using the derived $CR = 0.11$ from the previous section the E_{oed}^{ref} can be calculated as:

$$E_{oed}^{ref} = \frac{p^{ref}}{CR} * ln(10) \tag{4.19}$$

with a p_{ref} of 300 kPa, as is used earlier and once again under the assumption that an m equals 1 holds for the oedometer test. This does mean that the E_{oed} is slightly overestimated at lower stresses, as can be seen in Figure 4.6.

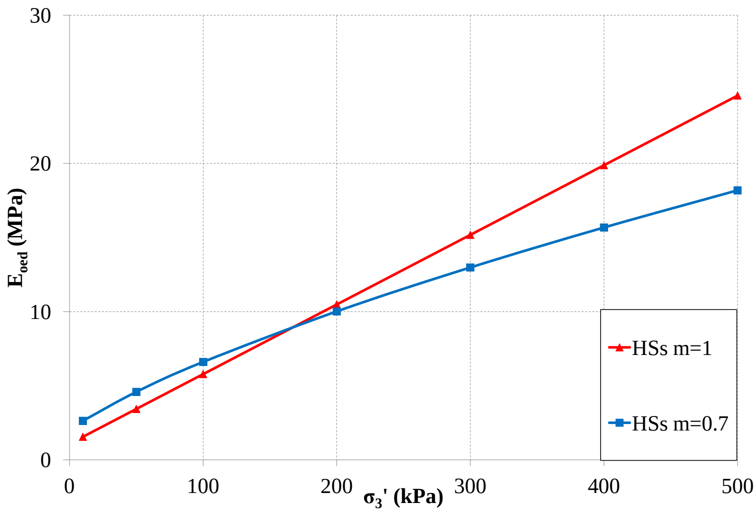

Figure 4.6: Oedometer stiffness for $m = 0.7$ and $m = 1$.

The choice is made to use $m = 0.7$, because of the importance of the E_{ur} and the input of one m value in the HSs. Since the deformations are dominated by the E_{ur} this deviation is considered acceptable. Please note that the unit of the horizontal axis σ_3' seems a bit unusual for an oedometer test. This is chosen for the consistent σ_3' dependence of the E moduli in the HSs model. As can be seen from Equation (4.5) this term is actually σ_3'/K_0^{nc}, thus explaining the overlap of both lines at approximately $300 \times 0.56 = 168$ kPa, rather than the reference stress level of 300 kPa.

The E_{50} is determined at the stress level $q_f/2$, preferably from drained triaxial tests. Since those were not available, isotropically consolidated undrained TA tests are used. The E_{50} is mainly used as a material parameter because it is easy to determine from an $\varepsilon - q$ plot, it is however difficult to state what this stiffness actually represents. The influence of both isotropic and deviatoric (preconsolidation) loading are present in this modulus. Therefore the choice is made to determine this modulus related to the E_{ur}. From the Plaxis manual [31] it is suggested to use a ratio of $E_{50} = E_{ur}/3$. This is comparable with the determined E_{50}^{ref} values from the laboratory tests, ranging from 12 to 17 MPa with an average value of 14.3 MPa at a reference pressure of 300 kPa, with the average $E_{ur}^{ref}/3 = 10.7$ MPa.

The stiffness parameters are closely related and in proportion to each other. The most influential one, for an excavation, is the E_{ur} with the G_0 a close second. The E_{oed} and E_{50} are best determined based on their ratio compared to E_{ur} and in accordance with the laboratory tests. An indication for the ratio between is E_{50}^{ref}:E_{oed}^{ref}:E_{ur}^{ref} = 3:2:10. The G_0^{ref} should be less than $\frac{5E_{ur}^{ref}}{1+\nu_{ur}} \approx 4E_{ur}^{ref}$.

4.3.3 Flow parameters

Pore pressures are important for the geomechanical behaviour and the numerical calculation. Permeability coefficients are derived from the laboratory tests. They result in average values of $c_v = 3.1 \times 10^{-8}$ m^2/s and $k_v = 2 \times 10^{-11}$ m/s.

Pore water pressures were measured for over a year. The data gathered can be used to estimate the response of the pore water pressure to changes in water level. With a low permeability it is expected that a change in water conditions has a delayed effect. Figure 4.7 shows the pore water pressures in one of the piezometers at the centre of the trial excavation.

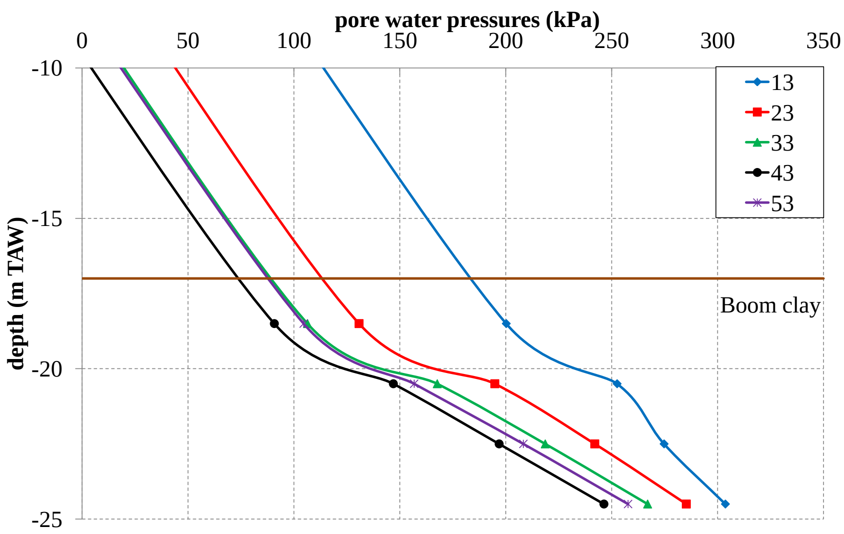

Figure 4.7: Response of pore water pressures due to drainage over time. The different lines represent the number of days since start of the drainage, t_0 = 05-05-2014.

At reference day 0, the water level was lowered. The coloured lines indicate the response over approximately the next 50 days. The Boom clay layer starts around -17 m TAW. The upper metres of the Boom clay show a rapid response to the change in water level. This indicates that the permeability of the (weathered) top layer is higher than the ones below. An increase in the permeability coefficients is also supported by the presence of fissures (Schittekat et al. [36], Dehandschutter et al. [9]). To incorporate this response properly in the calculation a distinction between the long term and direct response of the pore water pressures should be made. The long term response is governed by the permeability coefficient and the direct response, specifically due to stress relief, is modelled using the Skempton coefficients.

4.3.3.1 Permeability coefficients

Based on the field measurements and literature it was concluded that the top layer of the Boom clay is significantly more permeable than the other layers. The k value was increased, thus representing a higher permeability, to approximately 1×10^{-3} m/day. This is approximately the upper boundary for the permeability of a clay. The deeper layers of the Boom clay have a lower permeability, they are not weathered nor influenced by the trial excavation. For those layers the k value is determined directly from the laboratory tests, i.e. $k = 1 \times 10^{-6}$ m/day. Between the top and bottom layer a transition zone, regarding permeability is defined with $k = 1 \times 10^{-5}$ m/day. In the next chapter the magnitude of these values is supported with the comparison between calculation and the field measurements.

4.3.3.2 Skempton coefficients

Excavating will lead to a stress relief on the Boom clay. Due to the low permeability of clay it is important to estimate what the effect of a stress change is on the pore water pressures. Skempton [38] expressed this using pore pressure coefficients in his well know equation:

$$\Delta u = B\left[\Delta\sigma_3 + A(\Delta\sigma_1 - \Delta\sigma_3)\right] \tag{4.20}$$

Under isotropic conditions Skempton defined B as:

$$\frac{\Delta u}{\Delta\sigma_3} = \frac{1}{1 + (nC_v)/C_{sk}} = B \tag{4.21}$$

with the porosity n, the compressibility of the voids C_v and the compressibility of the soil skeleton C_{sk}. If a soil is fully saturated with water $C_v = C_w$ and $C_w/C_{sk} \approx 0$ since the compressibility of water is generally much lower than that of a soil. This results in B = 1 for fully saturated soils. If the soil is completely dry the $C_v = C_{air}$, where the compressibility of air is much higher than the C_{sk} resulting in $B = 0$. The Skempton B varies (non-linearly) with the degree of saturation, S (Holtz & Kovacs [16]). Small changes in saturation can result in a significant decrease of B as Table 4.5 displays.

Soil type	**S = 100 %**	**S = 99 %**
Lightly OC clay	0.9988	0.930
Stiff OC clay	0.9877	0.51
Very stiff OC clay, at high pressure	0.9130	0.10

Table 4.5: Skempton B values at complete and nearly complete saturation. After Black & Lee [4].

The Skempton A value is obtained from the stress paths of the soil in undrained loading. This value is not a constant, it varies with stress level. Skempton presented the following A_f values, A at failure, for various clays displayed in Table 4.6.

Type of clay	A_f		
Normally consolidated	$\frac{1}{2}$	to	1
Lightly OC	0	to	$\frac{1}{2}$
Heavily OC	$-\frac{1}{2}$	to	0

Table 4.6: Skempton A_f values for clays. After Skempton [38].

The Skempton A can be determined from undrained TA tests, assuming $B = 1$. When considering the stress paths in a $s' - t$ plane , $s' = (\sigma_1' + \sigma_3')/2$ and $t = (\sigma_1' - \sigma_3')/2$, it useful to rewrite Equation (4.20) to:

$$\begin{aligned} \Delta u &= \Delta(s - t) + 2A\Delta t \quad \rightarrow \\ \Delta s' &= \Delta s - \Delta u \quad \rightarrow \\ \Delta s' &= \Delta t(1 - 2A) \quad \rightarrow \\ A &= \frac{\Delta s' - \Delta t}{2\Delta t} \end{aligned} \tag{4.22}$$

This indicates indeed a varying Skempton A at different stress level, as is also seen in the effective stress path (ESP) displayed by the black points in Figure 4.8 (a).

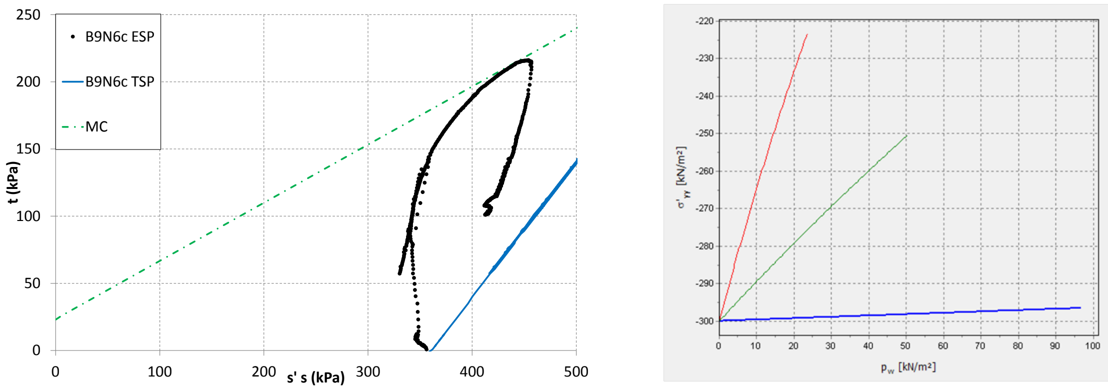

(a) Total and effective stress path with MC failure line from TA test on Boom clay sample.

(b) Influence of B=0.3 (red), B=0.6 (green) and B=1 (blue) on pore water pressures.

Figure 4.8: Determination and effect of Skempton coefficients.

Ideally this would be incorporated in the numerical calculation. The Skempton A cannot be adjusted in Plaxis, but the Skempton B coefficient can. This is therefore used to incorporate the influence of a more permeable top layer. The effect of varying the Skempton B value is checked with the SoilTest tool. The in situ stress state is approached with an isotropic stress of 300 kPa. Then a stress decrease of 100 kPa, similar to an excavation step, is applied. Figure 4.8 (b) shows the change of pore water pressures with different B values.

The exact magnitude of the B value is based on the changes in pore water pressures caused by the excavation steps. It was determined which percentage of stress change was transferred to a change in pore water pressures. The determination of these magnitudes is illustrated with the field data, shown in the next chapter.

4.4 Summary

This chapter described the investigated aspects for the numerical modelling of the trial excavation. The selected material models for the numerical calculation were discussed. The derivation of the numerical parameters was explained and the values are presented. The used parameters are summarised in Table 4.7.

Symbol	Property	Unit	Value/Range
c'	Effective cohesion	kPa	20
φ'	Effective friction angle	^{o}	26
ψ	Dilatancy angle	^{o}	0
E_{50}	Secant stiffness for drained TA test	MPa	8 - 12
E_{oed}	Tangent oedometer stiffness primary loading	MPa	6 - 9
E_{ur}	Unloading/reloading stiffness	MPa	24 - 48
G_0	Initial shear modulus	MPa	110 - 180
$\gamma_{0.7}$	Shear strain at which $G_s = 0.722G_0$	-	1 - 3 $\times 10^{-4}$
p_{ref}	Reference stress level	kPa	300
m	Magnitude of stress dependency	-	0.7
ν_{ur}	Poisson's ratio for unloading/reloading	-	0.3
K_0^{nc}	K_0 value for normally consolidated state	-	0.56
R_f	Failure ratio q_f/q_a	-	0.8

Table 4.7: Numerical parameters for the HSs model

Chapter 5

Calculation of trial excavation

This chapter provides additional information on the numerical calculation. Features and choiches in the model are explained and a selection of calculation results is presented. The attempt was to keep calculation as simple as possible, but close to reality. The program Plaxis2D, version AE.02 was used for the numerical calculations.

5.1 2D axisymmetric approximation

Because of the trial excavation's octagonal shape, it was approached with a 2D axisymmetric model. In this type of model a 2D radial cross section is defined, representing 1 radian of the rotation around the symmetry axis. It can be argued that 3D model is more suitable, especially regarding the deformations of the sheet piles. These are difficult to model accurately in a 2D axisymmetric calculation due to the overestimation of hoop forces, since the pit is modelled as a perfect cylinder. There are however some disadvantages associated with a 3D model. The main disadvantage is the significantly longer calculation time of a full 3D model. Figure 5.1 displays the 2D axisymmetric numerical model of the trial excavation.

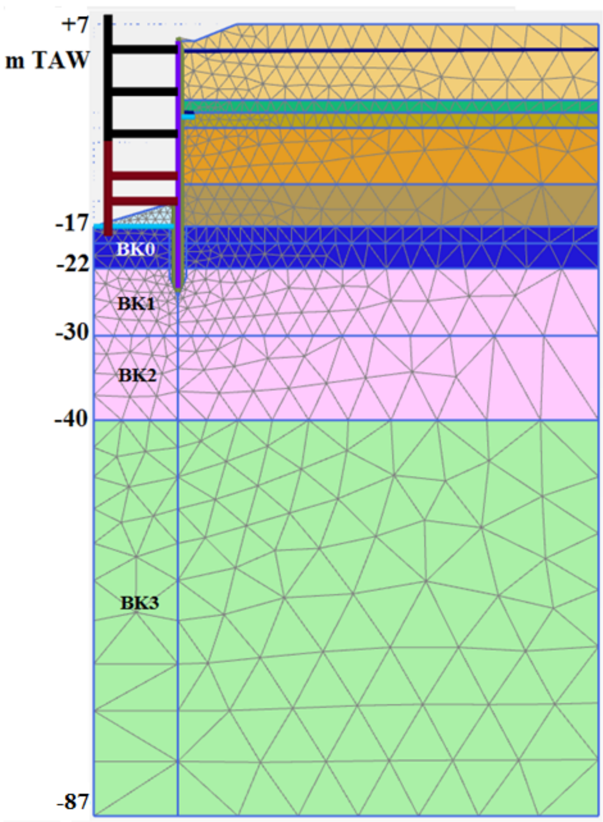

Figure 5.1: 2D axisymmetric model of trial Oosterweel trial excavation. The Boom clay is divided in three layers, BK0-3

The model simulates the trial excavation to a depth of almost a hundred meters. This choice is made to see if the model behaves properly at large depth. The effect of the installation and excavation will be negligible from a depth of 20 metres below the sheet piles, but it is interesting to see if this is captured properly in the model. The thick line at the top in Figure 5.1 represents the initial water level, at +4 m TAW. Struts are represented with the horizontal T's. The thick vertical line is the sheet pile and interface. Drainage is modelled with the light blue lines, one at the bottom and around -4 m TAW.

5.1.1 Construction phases

The excavation process covers more than a year, with almost forty stages in the calculation. The most important events during the excavation are:

- installation of the sheet piles
- drainage
- installation of struts
- excavation steps

These events are implemented in the construction stages. For the installation of the sheet piles a volume expansion was implemented. This simulates the increase in pore water pressures due the installation effects. The drainage both inside and outside the trial excavation were modelled with drains with a fixed head.

The calculation options for a phase can be chosen in Plaxis, for a more detailed explanation reference is made to the Plaxis manual [31]. The plastic option is the most simple one, without time dependency. Time is included in the consolidation option. All steps in which soil is excavated and after which the water level is changed are calculated with the consolidation option, the others with the plastic option. As calculation method Undrained(A) is chosen. This is done because it allows for consolidation and (the most accurate) calculation of pore water pressures. It is noted that the undrained behaviour is modelled using effective parameters for strength and stiffness. This is however preferred over the use of Undrained(B) since this option removes the stress dependency of the stiffness moduli entirely.

To model the pore water pressures a phreactic calculation, values from the previous phase or a steady state flow calculation can be chosen. Phreatic conditions are used in the stages before any drainage was applied. After drainage steps the default calculation option is to use the pressures from the previous phase. When the water level is changed due to drainage, then the steady state groundwater flow option is applied.

5.2 Implementation of the soils

The soils are categorised based on the geology determined from the reference literature and site investigations by RoTS [40], the tender company of W+B and Grontmij for the Oosterweel project. For the sands the HSs model is used and for the Boom clay both the HSs model and the GHS. It is assumed that all soil layers are homogeneous.

5.2.1 Top layers

The top layers consist mainly of sands, with a thin clay layer in between. For a description of stratigraphy of these sand layers is referred to Jacobs et al. [19]. The HSs parameters for these layers are taken from the research from RoTS [40]. These parameters were not further analysed, since the main interest is the Boom clay.

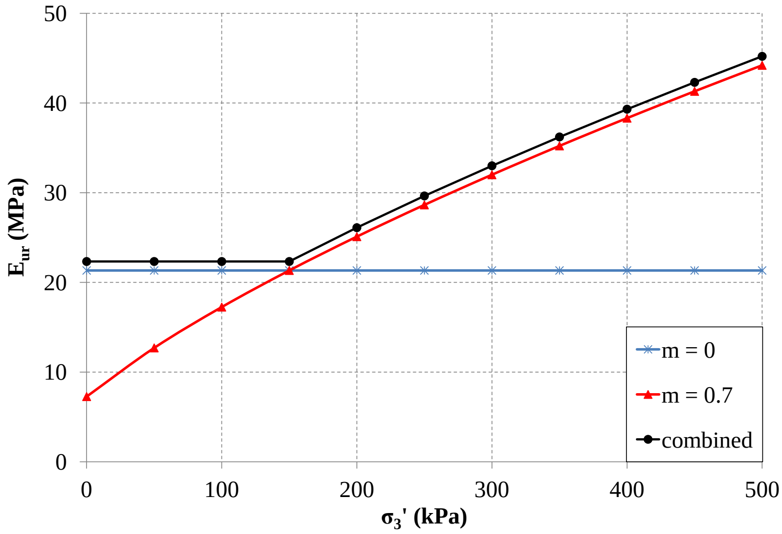

Figure 5.2: Derivation of a suitable cut-off value for the E_{ur} for the intersection between a layer with m=0 and m=0.7

5.2.2 Boom clay

The used parameters have been extensively discussed in the previous chapter. Figure 5.1 displays the Boom clay divided in 3 layers. The choice for this division is based on the geomechanical subdivision mentioned in the first chapter (Schittekat [36]) and the changes in permeability with depth. The differences between this division and the one proposed by Schittekat or the geomechanical subdivision (Table 2.3 on page 6) is that only three layers are distinguished, instead of four. No clear indications for the distinction between the layers between -22 and -40 m TAW was found, so BK1* = BK2. Additionally only changes in flow parameters are applied between the layers in the model. No reduction of strength and stiffness parameters is applied. Another difference is that the layer changes for the trial excavation are chosen closer to the surface. The BK3 layer starts at -40 m TAW, which deviates from the value presented in Table 2.3. This was done because the Boom clay is closest to the surface at the trial excavation.

Layer	k_v (m/day)	B (-)
BK0	1×10^{-3}	0.3
BK1*	1×10^{-5}	0.6
BK2	1×10^{-5}	0.6
BK3	1×10^{-6}	1

Table 5.1: Flow parameters per BK layer.

The difference in flow parameters are shown between the layers are given in Table 5.1. Another important difference is the choice of $m = 0$ for the BK0 layer. The stiffness moduli should connect logically with the underlying layers. Therefore the relevant stress level for these moduli, σ_3' was checked in the calculations between BK0 en BK2. From these values a reference E_{ur} was determined for the BK0 layer. Figure 5.2 displays the transition of the stiffness moduli between those layers.

5.3 Results

Selected results from the numerical calculations are presented in this section. These provide some insight in the modelled final situation of the trial excavation. The full Plaxis2D calculations are available in Appendix III.

A comparison between the HSs and GHS model is presented, all the in final (current) phase of the trial excavation. In this section the calculation option with the power law base on mean effective stress, p' of the GHS is used. This is believed to be the most suitable choice in an excavation. See Section 4.2.3 and Equation (5.1) for more information on the GHS. Two main differences between both models are;

- $m = 0.7$ with the GHS for the entire Boom clay layer versus $m = 0$ for the top 5 metres for the HSs.
- different power laws for stiffness moduli, see Equation (5.1)

$$E_{HSs} = E_{HSs}^{ref}\left(\frac{A+\sigma_3'}{A+p_{ref}}\right)^m \qquad E_{GHS} = E_{GHS}^{ref}\left(\frac{(\sigma_p'+p')/2}{p^{ref}}\right)^m \tag{5.1}$$

The plots of the pore water pressures, Figure 5.3 are only shown for the HSs, because no big differences between HSs and GHS are present there. This was expected, since the generation of pore water pressures is dependent of the flow parameters, which are the same for the HSs and GHS model.

Note that the legend in Figure 5.3 (a) differs from (b) and that pressure is indicated with a negative value and suction with a positive value. In the sand layers, above -17 m TAW, hydrostatic pore pressures are displayed as expected. Underpressures are present in the Boom clay directly underneath and between the sheet piles. The underpressures in the Boom clay layers are clearly visible in 5.3.

Figure 5.4 (a) indicates a disadvantage of the change in stress dependency of the top two layers. Much higher shear strengths are mobilised near the boundary between BK0 and BK2. The GHS model shows a more gradual transition, which appears to be more realistic. A possible adjustment in the power law for the HSs can help remove this abrupt change. An example is given in Equation (5.2)

$$E_{ur} = \begin{cases} E_{fix} & \text{if } \sigma_3' \leq \sigma_{min}' \\ E_{ur}^{ref}\left(\frac{A\,+\,\sigma_3'}{A\,+\,p_{ref}}\right)^m & \text{otherwise} \end{cases} \tag{5.2}$$

The vertical displacements of both models are very similar, as can be seen in Figure 5.5. The reference stiffness parameters of the GHS have been derived from the HSs values and compared to the measurements. This agreement is therefore somewhat artificial, but achieved without the removal off stress dependency for the stiffness of the top layers in the GHS model. Total shear strain development, Figure 5.6, is also in correspondence. The largest shear strains are shown in the sand layers, the maximum γ_s values in the Boom clay layers are 3%.

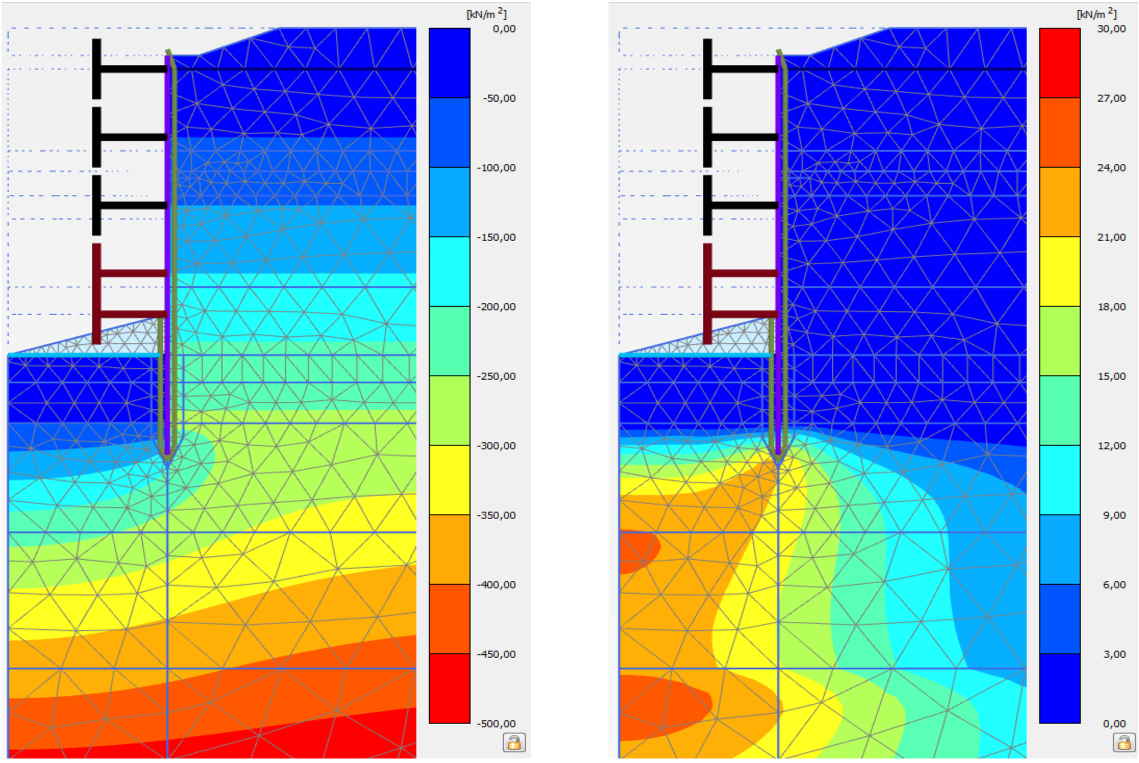

(a) Active pore water pressures **(b)** Excess pore water pressures

Figure 5.3: Pore water pressures in the final calculation phase.

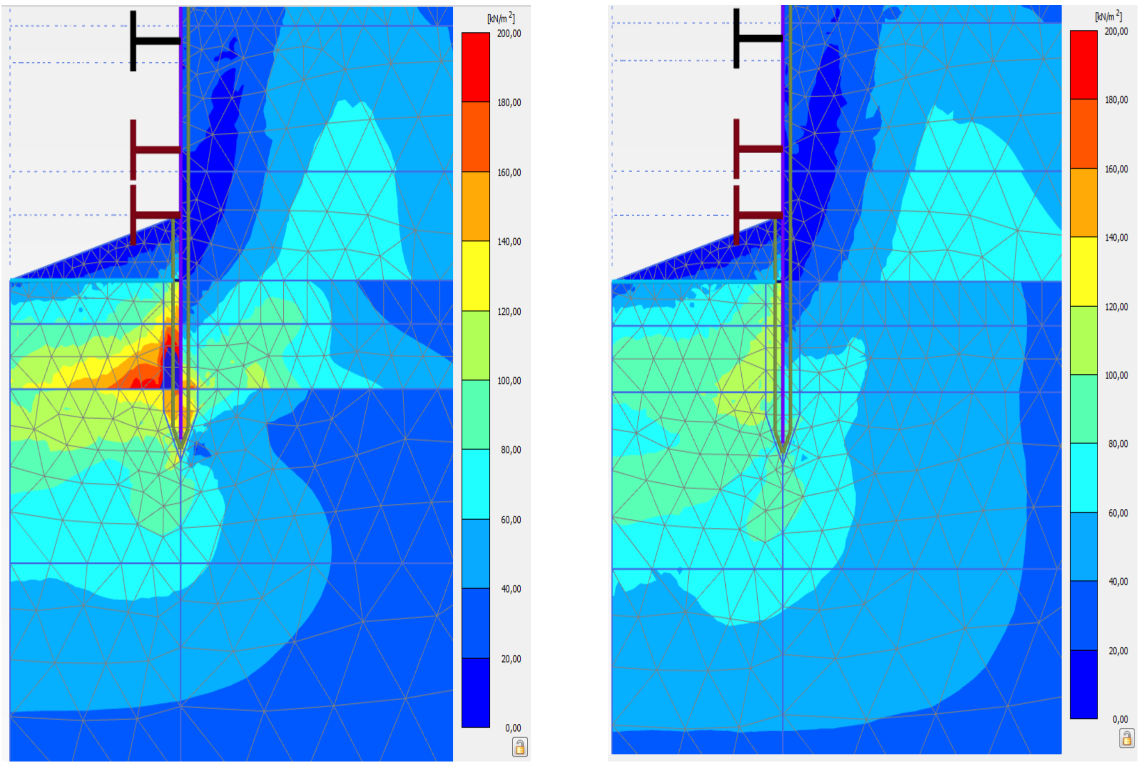

(a) HSs model **(b)** GHS model

Figure 5.4: Mobilised shear strength in the final calculation phase.

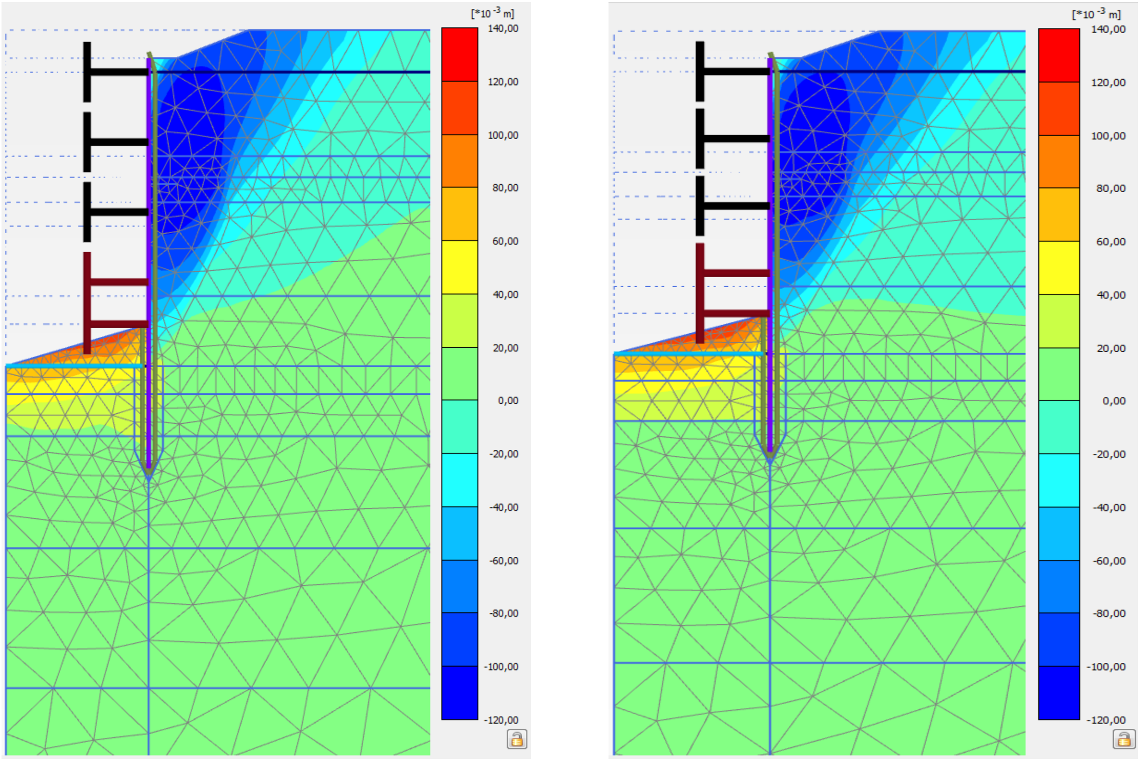

(a) HSs model (b) GHS model

Figure 5.5: Vertical displacements in the final calculation phase.

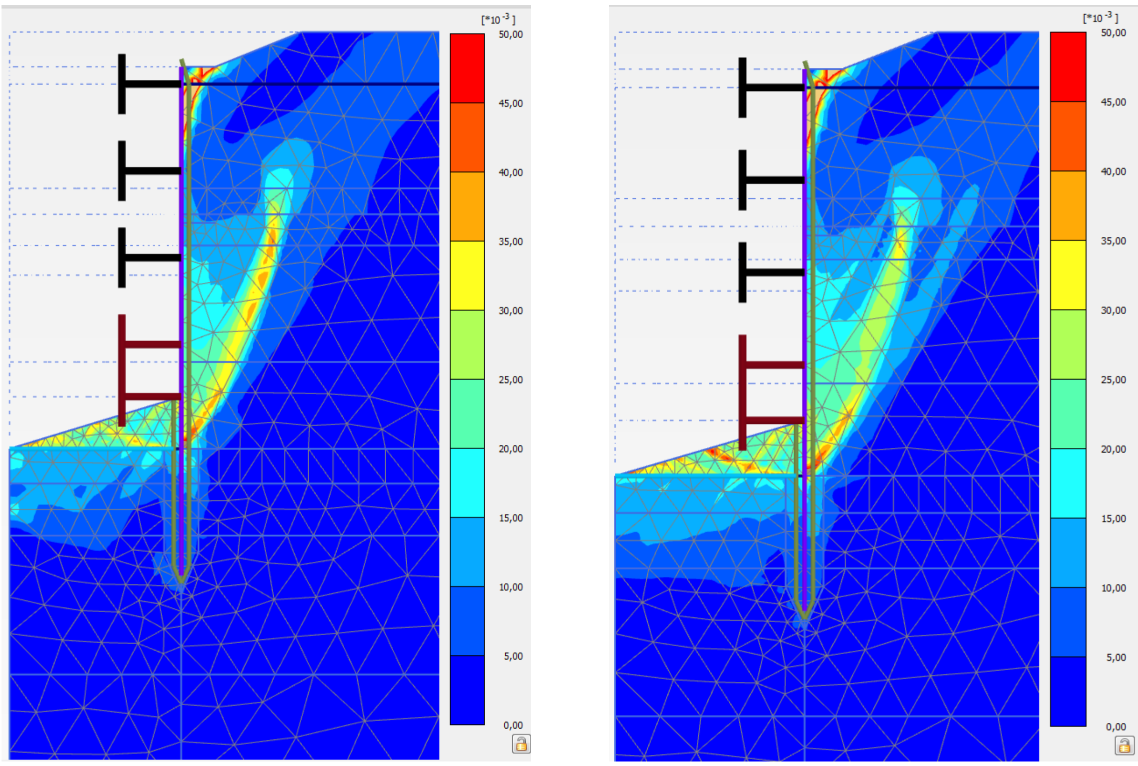

(a) HSs model (b) GHS model

Figure 5.6: Total shear strain in the final calculation phase.

The deformations of the sheet piles are presented below. They are relevant, because too large deviations from reality will influence the accuracy of the modelled soil behaviour. The same stiffness parameters for the sheet piles were used in both material models. The total displacements generated by the HSs model are slightly more than from the GHS model. These results are in the same order of magnitude as the field measurements. The next chapter will provide results over time compared to the field measurements.

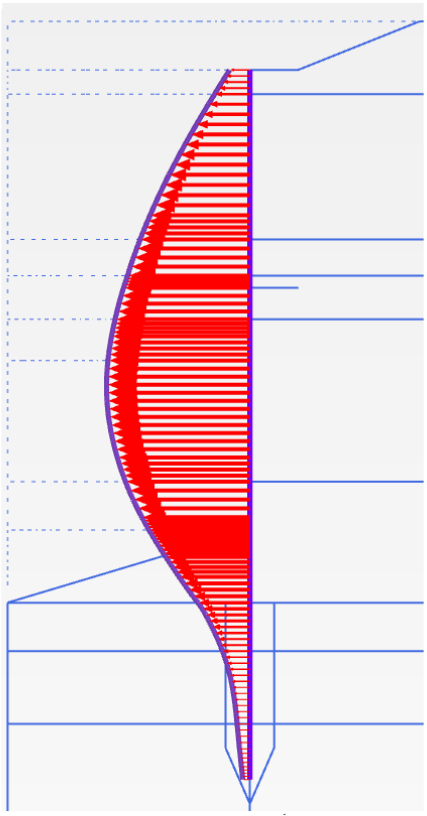

Total displacements u_x (scaled up 50.0 times)
Maximum value = -5.833*10^{-3}
Minimum value = -0.1182 m

(a) HSs model

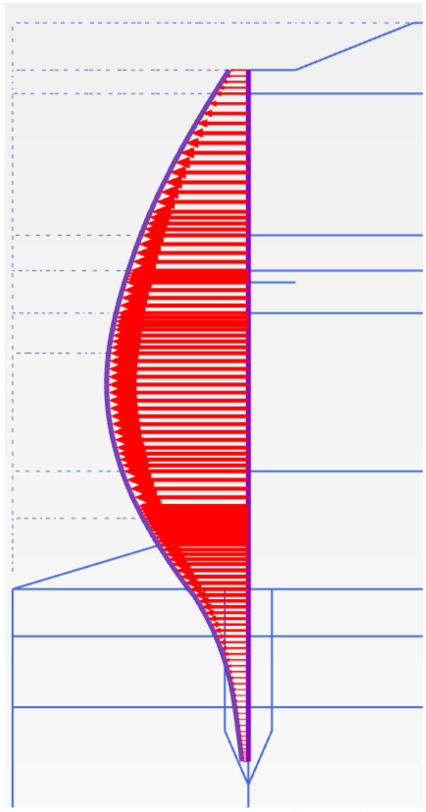

Total displacements u_x (scaled up 50.0 times)
Maximum value = -5.371*10^{-3}
Minimum value = -0.1202 m

(b) GHS model

Figure 5.7: Horizontal displacement of the sheet pile in the final calculation phase.

5.4 Summary

The features of the numerical model of the trial excavation have been given. The Boom clay is divided in three separate layers with a different values for the flow parameters. The Plaxis2D calculations are performed with the Hardening Soil model with small strain stiffness and the Generalised Hardening Soil model. An advantage of the HSs model is that the determined model parameters are derived from the laboratory tests. This provides a satisfactory model for the trial excavation. The GHS model is also suitable for the trial excavation, with the advantage of having fully stress dependent Boom clay layer. However the numerical parameter determination is not straightforward. The model was calibrated based on the HSs model and field measurements from the trial excavation.

Chapter 6

Interpretation of field measurements

This chapter presents the interpretation of field measurements from the Oosterweel trial excavation. Observations from the site visit and some initial in situ tests are presented. Then data of the measured pore water pressures and displacements are presented and discussed. This chapter aims to provide a clear interpretation of the field data. The gathered insights are compared to the results from the numerical calculation. Note that this chapter presents pore pressure with positive values, i.e. a pore pressure of 100 kPa is represented as 100 kPa and suction of 50 kPa is indicated with $u = -50$ kPa.

6.1 Site observations

A part of the trial excavation has been excavated to the Boom clay. This allowed for an inspection of the soil and some in situ tests. Figure 6.1 (a) displays the bottom of the trial excavation, where clay has been freshly excavated. The clay displays a block structure, which is remarkable. This structure might be caused by the excavation with a spade. An example of a block of Boom clay is shown in Figure 6.1 (b). Manual Shear Vane (SV) and Pocket

(a) Freshly excavated Boom clay

(b) Blocks after excavation

Figure 6.1: Boom clay from the trial excavation.

Penetrometer (PP) field tests have been performed on the Boom clay at the surface. Only a few tests were performed, but these values are used as an indication. The results are presented in Table 6.1, which shows the units read from the tests recalculated to undrained shear strengths. It is emphasised that these values are prone to error and should only be used as an approximation.

The values in Table 6.1 are relatively high s_u values, when it is considered that the effective vertical stress on these samples is practically zero. It appears that the Boom clay is able to retain pore under-pressures, resulting in a higher undrained strength. When it is disturbed the Boom clay will lose these favourable characteristics. This effect is difficult to quantify, but useful to consider when excavating Boom clay.

Sample	Saturation	X_{TV} (-)	s_u (kPa)	PP (kg/cm^2)	s_u (kPa)
7 days old	moist/dry	6	64	1.5	74
Remoulded	moist/dry	2	21	0.5	25
Fresh	wet/moist	9	97	2.0	98

Table 6.1: Results Boom clay manual SV and PP tests.

6.2 Pore water pressures

The pore pressures were measured with two types of devices; piezometer tubes and BAT piezometers. The piezometers will be indicated with the abbreviation P and then the number of the piezometer tube for convenience, e.g. P1.1. Similarly the BAT sensors are denoted as B1, the depth of the sensors is given in metres TAW. The piezometer tubes are installed in a cylindrical steel casing (∅ = 110 mm) filled with gravel. Water can easily infiltrate in the coarse gravel. The resulting level of the water in the cylinder is measured in the tubes. The BAT sensors are placed inside cones (∅ = 45 mm) which are in direct contact with the soil. Water infiltrates via a porous stone at the bottom of the device, which is then measured by the sensor. At two locations, in the centre and just outside the trial excavation, both piezometer tubes and BAT devices are installed at a similar location and depth. This allows for a comparison between the used devices.

Figure 6.2 displays the measurements from both devices over time. In general the BAT displays lower pressures than the monitoring well. This can be attributed to calibration of the device.

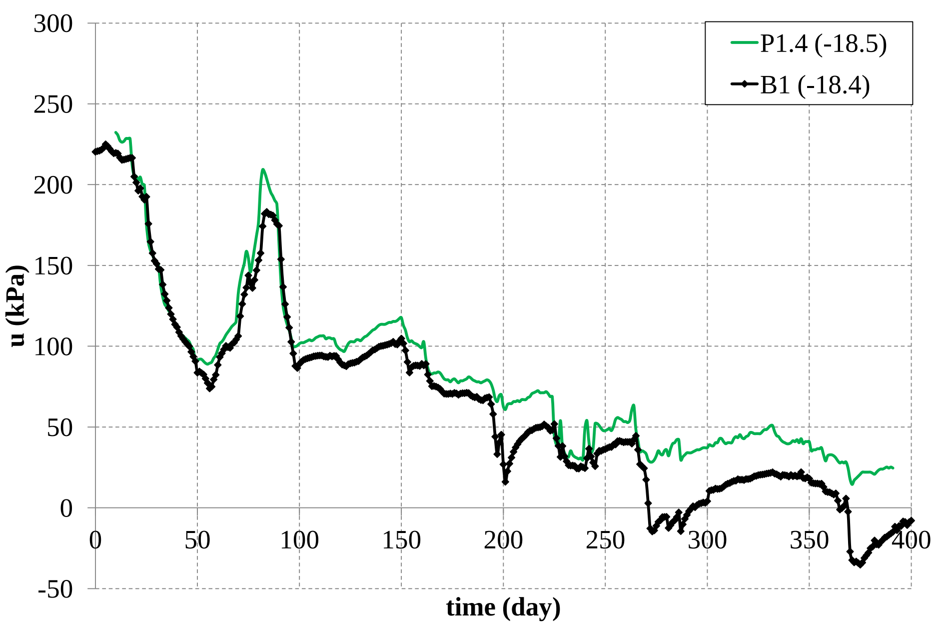

Figure 6.2: Comparison between piezometer tube P1.1 and BAT 1 at approximately -18.5 m TAW at the centre of the trial excavation, $t_0 = 28 - 04 - 2014$.

During the first 190 days the results from both devices are similar. After day 190 both measurement devices display different pore pressures. The piezometer tube displays a drop of circa 10 kPa versus 50 kPa from the BAT sensor. This can be explained by the difference in the measuring devices, but they were in accordance up to this point. The BAT sensor is apparently able to capture a more direct response of the pore water pressures where the piezometer tube is not.

A hypothesis is that the BAT sensor is in direct contact with the soil and pores. It is therefore better able to measure the direct reaction of a change in pressure. The piezometer tubes are not in direct contact with the clay, water infiltrates through the gravel around the sensors. They appear to react slower and more gradual. Figure 6.2 also shows that the BAT sensors measure suction, where the piezometer tubes do not, another significant difference. Over time both devices do seem to converge.

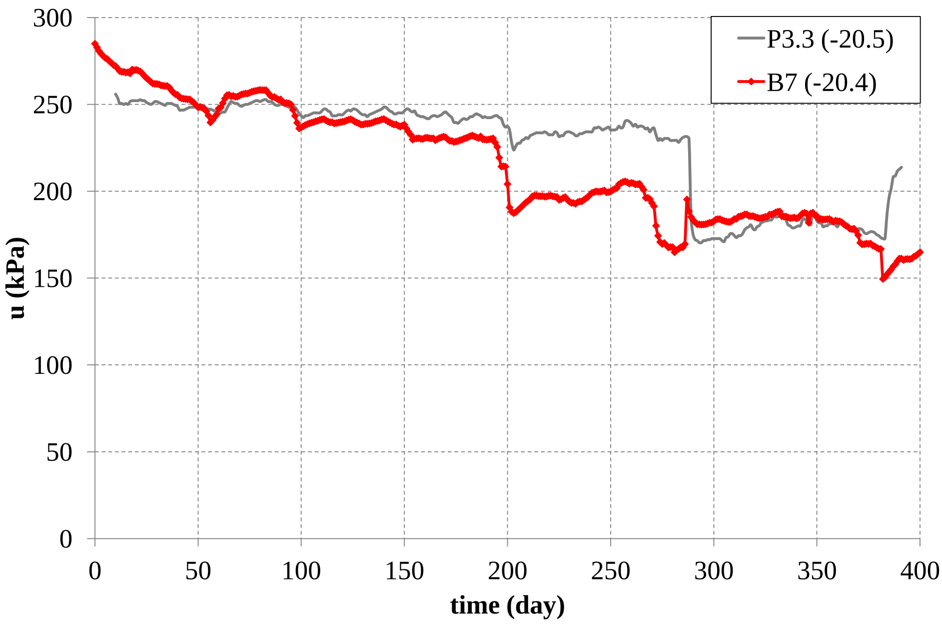

Figure 6.3: Comparison between piezometer tube P3.3 and BAT 7 at approximately -20.5 m TAW just outside the trial excavation, $t_0 = 28 - 04 - 2014$.

A similar pattern is observed from the piezometers just outside the trial sheet piles, P3.3 & B7 shown in Figure 6.3. Outside the building pit the effect of soil excavation is of less influence on the pore pressures. The biggest jumps are the drainage events. Around the 280 day mark the level outside the trial excavation was lowered with 8 metres, naturally resulting in a significant drop of the pore water pressures. At the end of the measurements a peak in P3.3 is observed, which is not shown in the BAT sensor. At this time the drain outside was stopped, but it is unclear why this results a much stronger response for P3.3.

Figure 6.4 on page 52 displays the depth trend of the pore water pressures measured in the centre of trial excavation. At the centre of the trial excavation only measurements from the piezometers are available over depth. The piezometers closer to the surface display a stronger response to the changes in water conditions than the piezometers at greater depth. The piezometer tubes at different depths do all respond without too much delay. This indicates that the construction stages affect the pore water pressures even at large depth in the Boom clay.

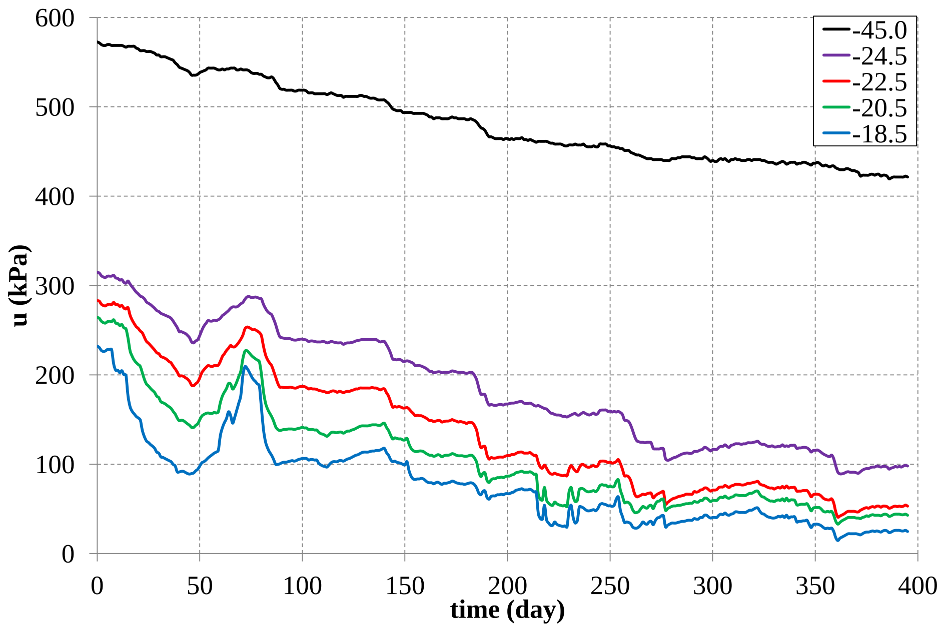

Figure 6.4: Pore water pressures from monitoring wells at the centre of the trial excavation over depth, $t_0 = 28 - 04 - 2014$.

6.3 Soil displacements

Extensometers are positioned in the centre of the trial excavation, anchored at circa 20 metres below the top of the Boom clay. Extensometer 2 is abbreviated as E2 and extensometer 4 as E4 for convenience. Figure 6.5 shows the total heave of the top of the Boom clay for E2 and E4. Note that a positive value of vertical displacement represents heave.

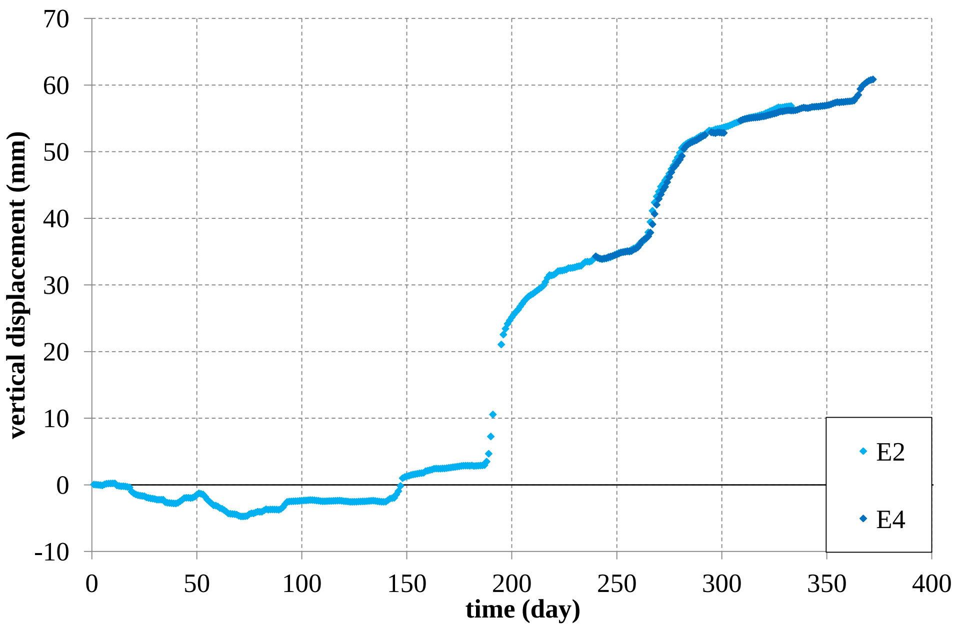

Figure 6.5: Vertical displacements top Boom clay layer, $t_0 = 24 - 04 - 2014$.

Figure 6.5 displays some absence of data around day 200. This was the excavation step to -12 m TAW and possibly the extensometer was damaged there. The depth trend of E2 is unreliable, as the comparison between Figures 6.6 (a) and (b) indicates.

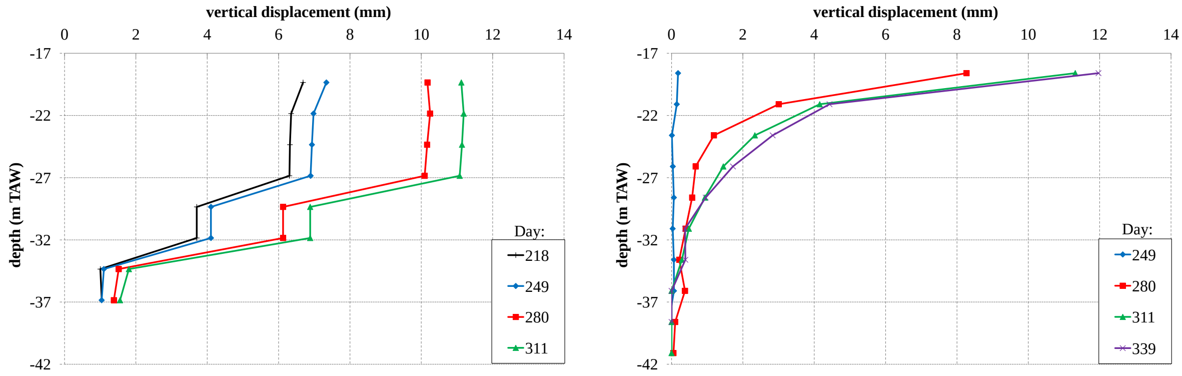

(a) E2 (b) E4

Figure 6.6: Differences in the modules of extensometers 2 and 4, $t_0 = 24 - 04 - 2014$.

Since 6.5 (a) shows an identical displacement over the top 10 metres, and then abruptly changes at the next sensor, this doest not appear to be realistic. The heave over depth from figures 6.6 (b), with a more displacements in the top layers and a more gradual decrease of decrease of heave over depth is more realistic. If an estimation of the heave over depth is required, this is best approximated by E4. E4 was installed after the problems with E2 were observed. The total heave from E2 was however still in accordance with E4.

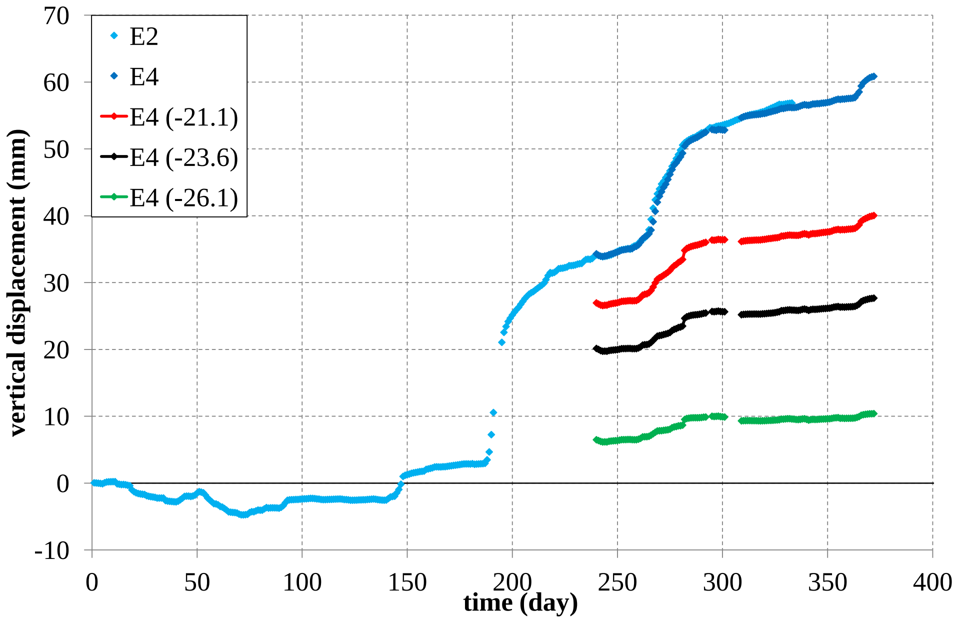

Figure 6.7: Vertical displacements over depth and time based on E2 and E4, $t_0 = 24 - 04 - 2014$.

Figure 6.7 shows both extensometers over time and depth. The exact placement of E4 is somewhat speculative, since the exact reference point could not be determined. They do provide an insight in the ratio between the heave development over depth and time. Observed is that most heave occurs in the top meters and almost no deformations below -35 m TAW are observed.

6.4 Comparison numerical model

Total heave and pore pressures inside the trial excavation over time are compared. An approximation of the maximum horizontal displacement of the sheet piles is also considered. It was not possible to compare and present all measured data, because the database was too extensive. These data are however available in Appendix II.

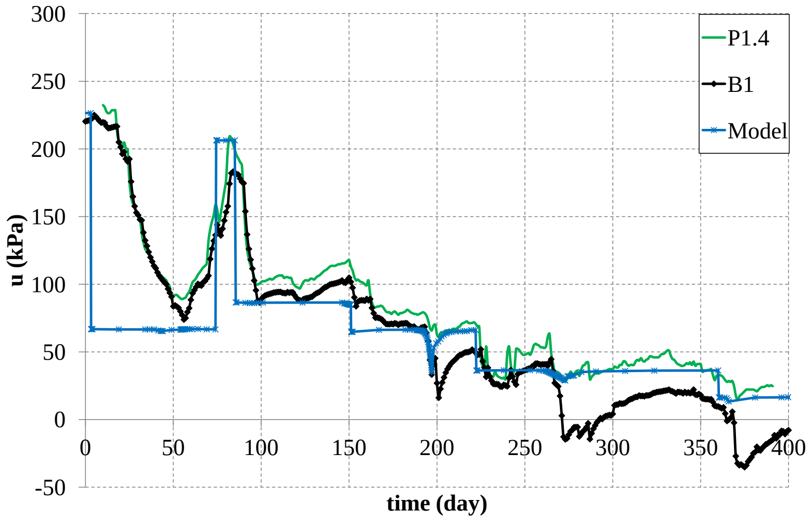

Figure 6.8: Comparison pore water pressures at the centre of the trial excavation and the numerical model.

The pore pressures are fitted, providing a similar trend as the field measurements. They are closer to the piezometer measurements than the BAT sensors. Overall the pore pressure response is properly captured, as can be seen in Figure 6.8.

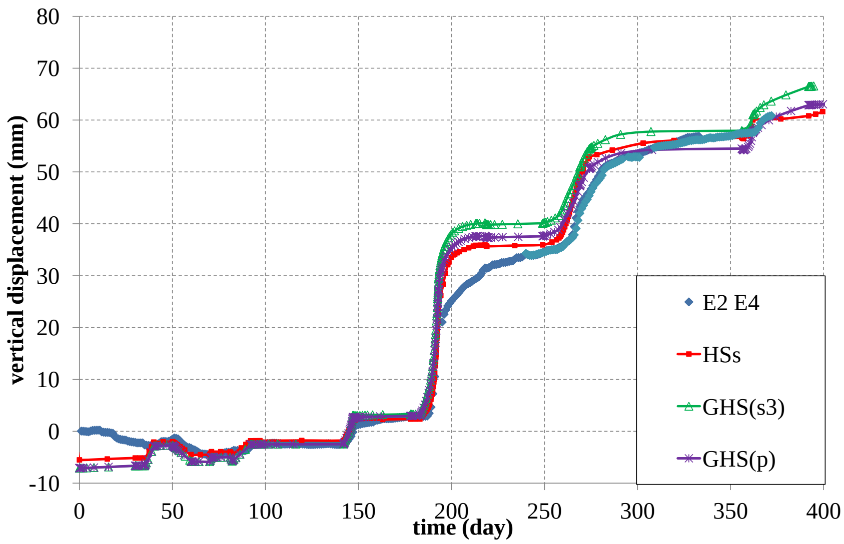

Figure 6.9: Vertical displacements top Boom clay layer compared to the numerical calculations.

The total heave was modelled accurately. The consolidation phases are not perfect but the trend and response over time works well for HSs model and both GHS options. The reference stiffness moduli for the GHS model were fitted with the HSs values and heave measurements. Figure 6.9 displays the results for $E_{GHS}^{ref} = \frac{4}{5} \times E_{HSs}^{ref}$ and a $m = 0.7$ over the full depth of the

Boom clay. This provided the best fit for the displacements. It was chosen not to fine tune this any further because it does not improve the model. The time for all events during construction are not exactly known and therefore difficult to model. Additionally some metres sand were still left in the trial excavation. This was taken into account, but the exact amount is unknown, reducing the value of an exact approximation.

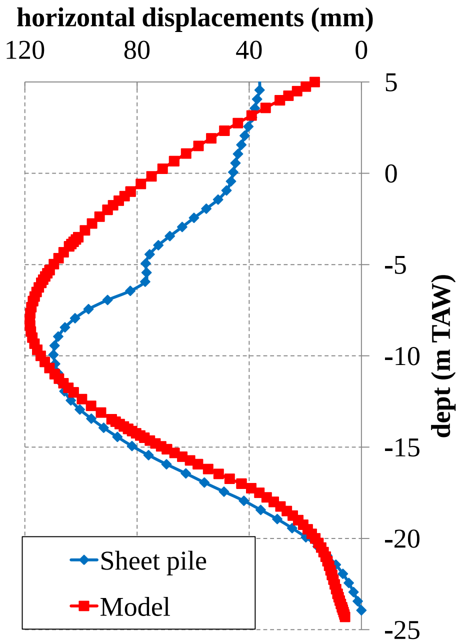

Figure 6.10: Comparison between the horizontal displacements of the sheet pile.

The horizontal deformations of the numerical model are roughly in the same order as the field measurements, which was found to be satisfactory. As mentioned the focus is on the Boom clay behaviour. To model the sheet pile displacements more accurately a 3D calculation is more suitable.

6.5 Summary

Freshly excavated Boom clay samples were inspected in the trial excavation. A block structure was observed and s_u values determined using pocket measurement devices. The pore pressures measurements differ between the piezometer tubes and the BAT sensors, especially quickly after excavation steps. Long term deformations are presented and compared with results from the numerical calculations over time. These are satisfactory approached with in the numerical calculation.

Chapter 7

Discussion

This chapter provides additional explanation on the choices made in this research. It explains the considerations for the interpretation of the geology and laboratory tests. Furthermore it focusses on the comparison between the field measurements and the numerical model. Finally the limitations will be discussed.

7.1 Geology and laboratory data

- The Boom clay in Antwerp is classified as heavily overconsolidated. The exact magnitude of the effect of this overconsolidation on the Boom clay's geomechanical behaviour is difficult to determine. Therefore it was chosen to use existing relationships (e.g. SHANSEP equation) and account for the OC state were possible. An interesting question regarding the preconsolidation stress is whether the full amount of stress is 'remembered' in its current state. Since this previous load was present over a million years ago, it might very well be that a part of the preconsolidation stress was not preserved.
- Instead of dividing the Boom clay in five layers a division in three layers was chosen. This choice is based on the observed difference in hydro-mechanical properties of the Boom clay. A more permeable top layer and low permeable bottom layer from were found in the measurements. A layer in between was defined as a transition zone. No indication for reduced strength and stiffness parameters per layer was seen in the laboratory tests or field measurements. It could be argued that the top layers should have some reduced strength and stiffness because of weathering, this could however not be derived from the laboratory tests.
- The determination of unloading/reloading stiffness from the oedometer tests is not indisputable. It is derived over the full unloading range, because this is closest to what will happen when the clay is fully excavated. Choosing the full range also provides the lowest E_{ur} values. Based on the results from the performed laboratory tests it is advised to determine the E_{ur} from triaxial tests. It is interesting to see how oedometer and triaxial tests match when the unloading/reloading steps are performed in the same strain range. The derived E_{ur} values should be comparable. This was however not the case for the performed laboratory tests.

7.2 Choices numerical model

- The numerical calculation is kept as simple as possible, while remaining close to reality. This was especially important because of the numerous stages during construction and the calibration of the numerical parameters. A disadvantage of this simplification is that the pore pressures are not fully accurate in the early stages of the calculation. If this is desirable the pore water pressures can be improved by defining different permeabilities in soil clusters before and during excavation.
- The Hardening Soil model with small strain stiffness was found to be a suitable model for the trial excavation. The inclusion of small strain stiffness results in more realistic soil

displacements. The GHS proved to be useful too, but the lack of theoretical background behind the model is a point for improvement. It was unclear how to derive suitable reference stiffness parameters from the laboratory tests because of this. The used parameters were determined based on the HSs reference values and calibrated with the measurements from the trial excavation.

- The HSs model should however be used cautiously in excavations, because of the stiffness reduction at lower stress levels. This is caused by the change of direction of the principle stresses. In the initial state the the vertical stress σ_v is the major principle stress, σ_1 and the horizontal stress, σ_h is equal to the minor principle stress, σ_3 After excavation σ_v becomes zero and thus $\sigma_3 = 0$ and $\sigma_1 = \sigma_h$. This leads to an unwanted decrease in the E moduli, because the HS(s) power law formulation which depends on σ_3. The use of the GHS model helps to reduce this effect. Additionally the option for removal of the stress dependency of the top layers is possible, but this boundary should be properly implemented in each specific calculation.
- The small strain stiffness modulus was approximated based on the stiffness reduction curve from Hardin & Drnevich ([15]). This could be done because of the accurate data points close to the small strain range. Secant shear moduli were determined from the start of unloading/reloading and plotted, all values combined were fitted with the stiffness reduction curve. This is an experimental method but the values appear to be realistic. Additionally the $\gamma_{0.7}$ can be derived from these data. If no tests are available a $\gamma_{0.7}$ in the range of 1 to 3 $\times 10^{-4}$ is advised. Furthermore numerous correlations are proposed by Benz [3] to estimate small strain stiffness parameters.

7.3 Comparison field measurements and numerical calculation

- Different pore water pressures are measured by the piezometer tubes and BAT-sensors. This might be caused by a different hydraulic behaviour at system level, the trial excavation and a micro level, the soil fabric. The macro level is displayed in the numerical model. The micro scale pore pressures are present in the soil's pores, which appears to be observed in the BAT sensors. The exact implications of this distinction are very difficult if to quantify. To investigate these processes and interactions is beyond the scope of this research.
- When modelling the field measurements it was not attempted to exactly match every small change. The processes should be in accordance, rather than matching every detail. The results from the field measurements should be carefully compared due to interaction of many processes. It was however achieved to perform a numerical calculation that combined all these aspects and matched the field measurements.
- Some selected measurements and numerical results were compared in the previous chapter. However many more data are available, which could not be presented because of time constraints. These data could be used for other project related to the Boom clay. Since the vast amount of unique information from this trial excavation the data and analyses are stored and can be used for further research.

7.4 Limitations of this research

- The geotechnical and numerical parameters of the Boom clay layers are assumed to be isotropic. Though reference articles (Piriyakul [30], Marivoet et al. [25]) have mentioned differences in horizontal and vertical permeability of the Boom clay. The influence of anisotropy is outside the scope of this work.
- Calculations and measurements are based on the trial excavation. It is unclear how these results translate to excavation of a different size. The derived geotechnical parameters are

succesfully used to model the trial excavation and it is interesting to see how they perform on other excavations.

- No analysis is performed on the sheet pile deformations in the trial excavation. The largest deformation was approximated. This was decided due to some problems with the installation of struts and therefore options to model this effect. Also the choice for a 2D axisymmetric approximation is less suitable to model sheet pile deformations. When these need to be modelled more accurately it is sensible to perform a 3D numerical calculation.
- The small strain stiffness is experimentally approximated and not directly measured. As is mentioned in the previous section, this was preferred over not including small strain stiffness at all or choosing a value based on correlations.
- In the trial excavation the Boom clay was not fully unloaded, as some metres of sand were left on top of the layer. This an unfortunate result of budget restrictions . This effect is included in the numerical calculations by leaving sand in the final excavation stage.
- The long-term behaviour of the Boom clay is not quantified. This was impossible, since many changes in stress and hydraulic conditions were made during the construction and monitoring. When the trial excavation is left undisturbed and is monitored for a longer time the long-term behaviour could be quantified.

Chapter 8

Conclusions and recommendations

The main aim of this research was to predict the geomechanical unloading behaviour of the Boom clay in an excavation. This was achieved by performing a desk study, by analysing the laboratory tests, by numerical calculations and finally, by interpreting the field measurements from the trial excavation. All these aspects combined provide a clear image of the Boom clay's geomechanical unloading behaviour.

8.1 Conclusions

The Boom clay is a heavily overconsolidated Paleogene clay. Its overconsolidation ratio (OCR) is 3.6 and the pre-overburden pressure (POP) equals 762 kPa at the top of the layer, which is situated in Antwerp. This overconsolidation affects the clay's characteristics, yet the extent of that influence is barely quantified. Most existing correlations and models tend to consider normally consolidated soils. While some experimental models have been developed, none are generally implemented in engineering practice.

Geotechnical and numerical Boom clay parameters were determined from the oedometer and triaxial tests. The ultimate effective strength parameters are found to be $c' = 20$ kPa and $\varphi' = 26°$. The undrained shear strength is analysed using the SHANSEP equation. The determined OCR influence is lower than reported in the reference literature (Ladd & Foott [24]). This implies that the undrained shear strength is not affected by the full preconsolidation stress or 'memory loss' of the Boom clay with respect to its preconsolidation stress. Unloading and reloading stiffness moduli were derived from both oedometer and triaxial tests. It was determined that the unloading/reloading stiffness can be more reliably derived from the triaxial tests. The average unloading/reloading stiffness, E_{ur} from the oedometer tests is two times lower than that of the triaxial tests and is considered to be too low. The strain ranges of the unloading/reloading steps in the oedometer tests were larger than those found from triaxial tests. This resulted in a lack of small strain stiffness influence in the oedometer tests, causing lower E_{ur} due to strain dependency of stiffness.

To model the trial excavation the small strain stiffness needs to be included in the numerical calculations. It is the Hardening Soil model with small strain stiffness (HSs), that is currently the most suitable option in Plaxis2D. To apply the HSs model to an excavation one should account for the change in minor principle stress, the σ'_3 direction when excavating. In this situation, this is achieved by removing the stress dependency of stiffness for the top 5 metres. Otherwise the reduction of σ'_3 to almost zero, would lead to an unrealistic stiffness reduction. The average E_{ur}^{ref} and a reference small strain stiffness modulus, G_0^{gef} are determined. The Generalised Hardening Soil (GHS) model adjusts the stress dependency equation of the HSs model, including the preconsolidation stress. Numerical calculations were performed with the GHS model. Its reference stiffness moduli were calibrated with the measured soil displacements. The GHS stiffness moduli can be derived by reducing the values from the HSs model by a constant factor.

The Oosterweel trial excavation proved to be a valuable source of information on the Boom clay's behaviour. The piezometers, extensometers and inclinometers provided data over both depth and time. The measured pore water pressures supported the theory of a weathered permeable top layer. Different swelling processes were identified and a continuous swelling over the construction phase was measured. A total heave of approximately 65 millimetres at the top of the Boom clay was observed, more than a year after the start of the excavation. Those measurements are satisfactorily modelled, with parameters derived from the laboratory tests, in the axisymmetric numerical calculation of the construction phase.

The geomechanical unloading behaviour of the Boom clay is complicated. Rather than displaying strictly drained or undrained behaviour a hybrid process is observed. During the construction phase the behaviour appears to reveal that it is predominantly undrained, due to the low permeability of the Boom clay. However on the full scale of the trial excavation water flow and changes in pore water pressures were observed. This indicates a distinction between behaviour on a very small scale (the clay's particle level) and macro behaviour (system level). This distinction is captured in the pore pressure measurements obtained from the BAT sensors and piezometer tubes. Pore water underpressures are held inside the small pore spaces of the clay, while the larger system water pressure adjusts more rapidly and no pore underpressures are measured. The geomechanical unloading behaviour is influenced by this difference in micro and macro structure, but it remains difficult to quantify.

8.2 Recommendations for further research

- It is recommended that constant rate of strain (CRS) oedometer tests are performed up to 4 MPa with unloading/reloading steps. Such tests can provide more insight into what happens in confined unloading rather than in an incremental loading test, since it provides continuous measurements. The increase of stress level provides a more accurate approximation of the virgin compression ratio, since the sample is then loaded far beyond the preconsolidation stress. Samples could be taken from the top 10 metres of the Boom clay, since that area was mainly affected by the trial excavation.
- Additionally incremental loading (IL) or CRS oedometer tests should be performed, starting from in situ stress states and the unloading the samples over a longer period of time. This would help to quantify the swelling behaviour over time. The sample is unloaded and then left for some weeks, until most of the swelling process has stopped. An alternative could be would be free swelling test on samples taken from the bottom of the trial excavation. This would show the swelling pressure that is present after excavation.
- Consolidated undrained triaxial tests with local (small) strain or bender measuring equipment to measure the G_0 are recommended. Ideally drained triaxial tests should be performed, but they are very laborious due to the low permeability of the Boom clay. If drained tests can be performed, is interesting to compare the results from these test to the results from the undrained tests.
- Compare the 2D numerical calculation to a 3D numerical calculation. This can be especially useful for the deformation of sheet piles and forces on structural elements. This could however, be time-consuming, especially when the model parameters need to be adjusted and the calculation consists of numerous stages. A 3D numerical calculation is, however, the most realistic approximation of reality.
- A desirable adjustment for the HSs and GHS model is the option of having a 'cut-off' for the stiffness in the power laws. This could be done be either specifying a minimum stress (σ_3') level or a lower boundary for the E modulus. This option would limit the unwanted reduction of stiffness with low σ_3' values. Additionally an adjustment of the HSs model's formula where the stress dependence is linked to the mean effective stress, p' rather than

to σ'_3 could be suitable for excavations. This is comparable to the GHS model's formula, but with the inclusion of effective strength parameters. If these adjustments are made, the reference moduli of the HSs and GHS would be easier to compare.

- The trial excavation should be monitored for another year without any significant changes in stress and water level. Even though the current measurements cover more than a year, many different changes were seen to influence the data. When the situation remains unchanged for a longer time, the time-dependent swelling process can be isolated. This is especially useful because the swelling remains difficult to quantify over time with the current measurements.
- Install extensometeres and piezometers in the Boom clay at the bottom of future excavations. These could remain there for the lifetime of the constructions, and provide valuable information on long term behaviour.
- Gather data on related projects in the Boom clay and compare the results. Similar deep excavations in the Boom clay have been performed, e.g. for the Kennedy tunnel and the Deurganckdock, both in Antwerp. The derived geotechnical parameters from this research could also be used to model these excavations. The comparison with available measurements from other sites can provide more insight into the effects for larger excavations.

Bibliography

[1] Atkinson, J. H. and Sällfors, G. (1991). Experimental determination of stressstrain-time characteristics in laboratory and in-situ tests. In *Proceeding of the 10th European Conference on Soil Mechanics and Foundation Engineering*, pages 915–956.

[2] Beerten, K., De Craen, M., and Wouters, L. (2013). Patterns and estimates of post-Rupelian burial and erosion in the Campine area, north-eastern Belgium. *Physics and Chemistry of the Earth*, 64:12–20.

[3] Benz, T. (2007). *Small-Strain Stiffness of Soils and its Numerical Consequences*. PhD thesis, Universität Stuttgart.

[4] Black, D. K. and Lee, K. L. (1973). Saturating Laboratory Samples by Back Pressure. *Journal of the Soil Mechanics and Foundations Division, ASCE*, 99(SM1):75–93.

[5] Brinch Hansen, J. and Mise, T. (1964). An empirical evaluation of consolidation tests with Little Belt clay. *Danish Geotechnical Institute*, (17):5–13.

[6] Brinkgreve, R. B. J. (2013). CIE4361: Behaviour of soils and rock. Lecture slides, Delft University of Technology.

[7] de Beer, E. (1971). Problèmes posés par la construction du tunnel sous l'éscaut a Anvers. Technical report.

[8] Decleer, J. (1983). Relationships Between Chemical, Physical and Mineralogical Characteristics of the Rupelian Boom Clay, Belgium. *Clay Minerals*, 18:1–10.

[9] Dehandschutter, B., Vandycke, S., Sintubin, M., Vandenberghe, N., and Wouters, L. (2005). Brittle fractures and ductile shear bands in argillaceous sediments: Inferences from Oligocene Boom Clay (Belgium). *Journal of Structural Geology*, 27(6):1095–1112.

[10] Deng, Y.-F., Tang, A.-M., Cui, Y.-J., and Li, X.-L. (2011a). Study on the hydraulic conductivity of Boom clay. *Canadian Geotechnical Journal*, 48(10):1461–1470.

[11] Deng, Y.-F., Tang, A.-M., Cui, Y.-J., Nguyen, X. P., and Wouters, L. (2011b). Laboratory Hydro-mechanical Characterisation of Boom Clay at Essen and Mol. *Physics and Chemistry of The Earth*, 36(17-18):1878–1890.

[12] dos Santos, J. A. and Correia, A. G. (2001). Reference threshold shear strain of soil. Its application to obtain an unique strain-dependent shear modulus curve for soil. In *Proceedings of the Fifteenth International Conference on Soil Mechanics and Geotechnical Engineering, Istanbul.*

[13] Femern (2014). Soil Models - Paleogene Clay. Technical report.

[14] Gromko, G. (1974). Review of Expansive Soils. *Journal of the Geotechnical Engineering Division, ASCE*, 100(SM2):1–17.

[15] Hardin, B. O. and Drnevich, V. P. (1972). Shear Modulus and Damping in Soils: Dsesign Equations and Curves. *Soil Mechanics and Foundations Division*, (SM7):667–692.

[16] Holtz, R. D. and Kovacs, W. D. (1981). *An Introduction to Geotechnical Engineering.* Prentince Hall Inc.

[17] Holtz, W. (1959). Expansive Clays - Properties and Problems. *Quarterly of the Colorado School of Mines*, 54(4):89–125.

[18] Honty, M. and De Craen, M. (2012). Boom Clay mineralogy qualitative and quantitative aspects. Technical report, SCK/CEN.

[19] Jacobs, P., Polfliet, T., De Ceukelaire, M., and Moerkerke, G. (2010). Kaartenblad 15 Antwerpen. Technical report, Geological Institute - Ghent Univeriesty.

[20] Janbu, N. (1963). Soil compressibility as determined by oedometer and triaxial tests. In *ECSMFE Wiesbaden*, pages 191–196.

[21] Kalantari, B. (2012). Foundations on Expansive Soils : A Review. *Research Journal of Applied Sciences, Engineering and Technology*, 4(18):3231–3237.

[22] Kondner, R. and Zelasko, J. (1963). A hyperbolic stress strain formulation for sands. In *Second Pan. Am. ICOSFE Brazil*, pages 289–394.

[23] Ladd, C. C. and De Groot, D. J. (2003). Arthur Casagrande Lecture - Recommended Practice for Soft Ground Site Characterization. In *12th Panamerican Conference on Soil Mechanics and Geotechnical Engineering.*

[24] Ladd, C. C. and Foott, R. (1974). New Design Procedure for Stability of Soft Clays. *ASCE Journal of Geotechnical Engineering.*

[25] Marivoet, J., Jacques, D., van Geet, M., Bastiaens, W., and Wemaere, I. (2009). Considerations on Upscaling of Hydraulic and Transport Parameters for a Plastic Clay Formation. Technical report, SCK/CEN.

[26] Mayne, P. W. and Kulhawy, F. H. (1982). Ko-OCR relationships in soil. *Journal of the Geotechnical Engineering Division, ASCE*, 108:851–872.

[27] Mertens, J., Vandenberghe, N., Wouters, L., and Sintubin, M. (2003). The origin and development of joints in the Boom Clay Formation (Rupelian) in Belgium. *Geological Society, London, Special Publications*, 216(1):309–321.

[28] MOW (2006). Masterplan Antwerpen. Technical report.

[29] NIRAS/ONDRAF (2001). Technical overview of the SAFIR 2 report. Technical Report December.

[30] Piriyakul, K. (2006). *Anisotropic Stress-Strain Behaviour of Belgian Boom Clay in the Small Strain Region.* PhD thesis, Ghent University.

[31] Plaxis (2014a). Material Models Manual. Technical report.

[32] Plaxis (2014b). Performance of the GHS. Plaxis internal document.

[33] Rijkers, R. H. B., Hemmen, B., Naaktgeboren, N. M., and Weigl, H. (2002). In-situ frost heave loads in ground artificially Hozen for tunnelling. In *Geotechnical Aspects of Underground Construction in Soft Ground*, pages 2–9.

[34] Schanz, T., Vermeer, P. A., and Bonnier, P. G. (1999). The hardening soil model: formulation and verification. *Beyond 2000 in computational geotechnics 10 years of PLAXIS. International proceedings of the International Symposium beyond 2000 in Computational Geotechnics*, page 281.

[35] Schittekat, J. (2001). *Engineering Geology of the Boom clay in the Antwerp area.*

[36] Schittekat, J., Henriet, J., and Vandenberghe, N. (1983). Geology and geotechnique of the Scheldt Surge Barrier, characteristics of and overconsolidated clay. In *8th International Harbour Congress*, pages 121–136.

[37] Schokking, F. and Nooy van der Kolff, A. N. (1995). History and geotechnical properties of the marine Boom Clay. In *DGF-Bulletin 11*, volume 7.141.

[38] Skempton, A. W. (1954). The Pore-Pressure Coefficients A and B. *Géotechnique*, 4(4):143–147.

[39] Skempton, A. W. (1964). The long-term stability of clay slopes. *Géotechnique*, 14(2):77–102.

[40] THV RoTS (2012). Geotechnisch basisrapport. Technical report.

[41] Vandenberghe, N. (1978). *Sedimentology of the Boom Clay (Rupelian) in Belgium.* Paleis der Academiën, volume 147 edition.

[42] Vinke, L., de Vos, L., Reyns, M., and van Zegbroeck, B. (2015). Deurganckdok Lock: extensive monitoring to evaluate and understand the swelling process of the Boom clay. In *Proceedings of XVI ECSMGE 2015.*

Appendices

Most of the appendices consist of Excel sheets and Plaxis calculations, which are poorly displayed on hard copy paper. Therefore it is decided to add the relevant sheets and analyses enclosed with a CD. A table of contents of the appendices is given below, with further explanation included in documents.